Mathematics

http://www.aimspress.com/journal/Math

AIMS Mathematics, 11(2): 3920–3956.
DOI: 10.3934/math.2026158
Received: 17 December 2025
Revised: 29 January 2026
Accepted: 04 February 2026
Published: 09 February 2026

Research article

Color image denoising under mixed multiplicative and Gaussian noise via group-sparse representation and SVTV regularization

Miyoun Jung*

Department of Mathematics, Hankuk University of Foreign Studies, Yongin 17035, Korea

* **Correspondence:** Email: mjung@hufs.ac.kr; Tel: +82-031-330-4261.

Abstract: Color image denoising under the simultaneous presence of multiplicative and Gaussian noise is challenging due to the differing statistical properties of the two noise types. We propose a variational framework that integrates an infimal-convolution-based data-fidelity term with saturation-value total variation (SVTV) and group-based sparse representation (GSR) regularization. By explicitly decoupling the multiplicative and Gaussian noise components, the data-fidelity term enables effective suppression of mixed noise. The two regularizers play complementary roles: SVTV promotes piecewise-smooth reconstructions while preserving edges, whereas GSR enhances fine details and textures and mitigates the staircase artifacts induced by SVTV. The resulting nonconvex optimization problem is addressed using a proximal alternating minimization strategy, with the alternating direction method of multipliers employed to efficiently solve the subproblems. A convergence analysis of the proposed algorithm is provided. Numerical experiments demonstrate that the proposed method consistently outperforms existing approaches for denoising color images corrupted by mixed multiplicative and Gaussian noise.

Keywords: color image denoising; multiplicative noise; Gaussian noise; group-based sparse representation; saturation-value total variation; proximal alternating minimization algorithm
Mathematics Subject Classification: 68U10, 65K10, 94A08, 65F22, 52A41, 90C26

1. Introduction

Images are often degraded by multiple noise types during acquisition or transmission. Image denoising is thus a fundamental problem in image processing, aiming to reconstruct a clean image from its noisy observation. In this work, we address the denoising of color images contaminated by mixed multiplicative noise and additive Gaussian noise. Multiplicative noise commonly arises in coherent imaging systems such as synthetic aperture radar (SAR) [1], ultrasound imaging [2], and laser imaging [3]. Owing to the coherent nature of these modalities, multiplicative noise can severely distort the acquired signal, often masking crucial structural details. Consequently, removing multiplicative noise is considerably more challenging than removing additive Gaussian noise. Additive Gaussian noise, in contrast, typically stems from sensor thermal fluctuations or variations in environmental illumination and affects all pixels uniformly. In many practical scenarios, both noise types occur simultaneously, complicating the denoising task. Furthermore, denoising color images is more challenging than grayscale restoration, as noise affects multiple channels and can disrupt inter-channel correlations. Effective methods must suppress noise while preserving spectral consistency to avoid color distortions. These factors make mixed-noise removal in color images particularly challenging.

Let $\Omega \subset \mathbb{R}^2$ be an open, bounded domain with a Lipschitz boundary, and let $u : \Omega \to \mathbb{R}$ denote the underlying clean image. The degradation model for the observed image f, corrupted by mixed multiplicative noise and additive Gaussian noise, is given by $f = u\eta + v$, where v denotes additive Gaussian noise distributed as $\mathcal{N}(0, \sigma^2)$ with zero mean and standard deviation σ, and η represents multiplicative noise following a prescribed distribution, such as Gamma or Rayleigh, depending on the imaging modality. In this work, we focus on Gamma-distributed multiplicative noise commonly encountered in SAR imaging. Specifically, η is assumed to follow a Gamma distribution with density given by [4]

$$g(\eta) = \frac{M^M}{\Gamma(M)} \eta^{M-1} e^{-M\eta}, \qquad \eta \geq 0, \tag{1.1}$$

where $M > 0$ is an integer parameter controlling the noise level and $\Gamma(\cdot)$ denotes the Gamma function. The mean of η is 1, and its standard deviation is $1/\sqrt{M}$.

For the removal of multiplicative Gamma noise, numerous filtering-based approaches [5–7] and variational models [8–10] have been proposed. Among filtering-based methods, the SAR block-matching 3D (SAR-BM3D) [7] is particularly notable for leveraging nonlocal self-similarity and wavelet-domain collaborative filtering. Despite its strengths, it is computationally demanding and may produce ringing artifacts near edges or block artifacts due to patch-based processing. Within the variational framework, Aubert and Aujol (AA) [8] proposed a model that couples a Gamma-based data-fidelity term with total variation (TV) regularization [11]. However, the nonconvexity of the data-fidelity term can lead to suboptimal solutions and high sensitivity to initialization. To address these issues, several convex variants have been proposed [9, 10, 12], often relying on logarithmic transformations or additional penalty terms. More recently, a few studies [13–15] have extended these variational formulations to color images, using the data-fidelity terms from [8,9,12]. Nevertheless, all these models focus solely on multiplicative Gamma noise and do not account for mixed-noise scenarios.

When mixed noise is present, a single data-fidelity term is often insufficient to achieve satisfactory denoising, and combining multiple fidelity terms has proven more effective. For example, linear combinations of L^1 and L^2 data-fidelity terms have been used to remove mixed impulsive and Gaussian noise [16, 17], and similar approaches have been proposed for mixed Poisson and Gaussian noise [18–20]. More recently, Calatroni et al. [21, 22] introduced TV-based models for denoising images corrupted by mixed salt-and-pepper and Gaussian noise, or mixed Poisson and Gaussian noise, using a data discrepancy defined via the infimal-convolution of the respective noise distributions. These fidelity terms have shown superior performance compared with simple linear combinations of individual noise-specific terms. Following this approach, [23] proposed an infimal-convolution-type data-fidelity term specifically designed for mixed multiplicative Gamma and additive Gaussian noise. In this work, we extend that model by incorporating a patch-based regularization to further enhance denoising performance.

TV regularization has been widely extended for color image restoration [24–26]. Jia et al. [26] introduced saturation-value-based TV (SVTV) in the HSV color space, which improves edge preservation and reduces color artifacts compared with RGB-based TV. This approach was subsequently applied to remove multiplicative noise and blur in color images [13]. However, SVTV suffers from staircase artifacts; to mitigate this, higher-order SV-based regularizers [14] were proposed. Nevertheless, local derivative-based methods still struggle to preserve fine textures and repeated patterns, often leading to detail smearing. To overcome these limitations, nonlocal methods exploiting image self-similarity have been extensively explored. The nonlocal means filter [27] aggregates similar patches based on global repetitiveness, and BM3D [28] extended this idea by using block-matching and 3D collaborative filtering, forming the basis for SAR-BM3D [7]. Nonlocal regularizations for inverse problems [29–31] generally outperform local methods, although inaccurate similarity weights can limit fine-detail recovery. Patch-based sparse representation methods, such as K-means singular value decomposition (K-SVD) [32], represent each patch using a learned dictionary. Despite its effectiveness, K-SVD ignores inter-patch self-similarity and is computationally intensive. Later studies integrated sparsity with nonlocal self-similarity [33–35] or employed low-rank modeling [36–38], with patches serving as the fundamental representation unit.

Zhang et al. [39] proposed the group-based sparse representation (GSR) model, which processes groups of similar patches to capture both local sparsity and nonlocal self-similarity using an adaptive group dictionary. This framework has demonstrated strong performance in image deblurring, inpainting, and compressive sensing, and has been extended to tasks such as image deblocking [40], low-light enhancement [41], and Cauchy noise removal [42]. Subsequent works combined GSR with low-rank and patch-based sparse methods [43–45]. Most existing GSR approaches for color images convert RGB to YCbCr and process only the luminance (Y) channel, which may be insufficient when noise affects all channels independently. To address this, [46] formed groups for each RGB channel separately, while [15] proposed a full-color GSR formulation that computes patch similarities directly on color patches across all channels, better preserving cross-channel correlations. Quaternion-based methods provide an alternative framework for color image processing by representing images as quaternion matrices, which inherently preserve inter-channel correlations. Representative approaches include low-rank approximation and matrix completion [47–49], as well as weighted nuclear norm and weighted Schatten p-norm minimization [50–52]. However, most quaternion-based methods do not explicitly exploit nonlocal patch grouping as in GSR. In this work, we adopt the full-color GSR framework [15] for mixed multiplicative and Gaussian noise removal, leveraging nonlocal self-similarity and adaptive sparsity to effectively preserve textures and cross-channel correlations.

The main contribution of this work is the development of a novel variational model for color images corrupted by mixed multiplicative Gamma and additive Gaussian noise. The model combines an infimal-convolution-based data-fidelity term with SVTV and full-color GSR regularization. The fidelity term decouples the multiplicative and Gaussian noise components, enabling their simultaneous removal. The two regularizers complement each other: SVTV smooths homogeneous regions while preserving edges, whereas GSR maintains fine textures and structural details across all channels and mitigates staircase effects. An efficient iterative algorithm based on alternating minimization and the alternating direction method of multipliers is proposed to solve the resulting nonconvex problem, with a theoretical convergence guarantee. The remainder of this paper is organized as follows. Section 2 reviews variational models for removing multiplicative or a mixture of multiplicative and Gaussian noise, along with SVTV regularization and the GSR framework. Section 3 introduces the proposed model and its optimization algorithm, with a convergence analysis. Section 4 presents experimental results and comparisons with existing methods, and Section 5 concludes the paper with a summary and discussion.

2. Preliminaries

2.1. Variational models for removing multiplicative or a mixture of multiplicative and Gaussian noise

We first recall a key property from [8]. *Let U and N be independent random variables with continuous density functions g_U and g_N, and let $F = UN$. Then, for $u > 0$, $g_N\left(\frac{f}{u}\right)\frac{1}{u} = g_{F|U}(f|u)$.*

Assume the data follows the multiplicative noise model $f = u\eta$, with f, $u > 0$, where η is Gamma-distributed with unit mean, as defined in (1.1). Then the conditional density of F given U is

$$g_{F|U}(f|u) = \frac{M^M}{u^M \Gamma(M)} f^{M-1} e^{-\frac{Mf}{u}}.$$

A maximum a posteriori (MAP) estimator yields the following variational formulation [8]:

$$\int_\Omega \left(\log u + \frac{f}{u} - \frac{M-1}{M} \log f \right) dx + \mu \Psi(u), \tag{2.1}$$

where $\mu > 0$ balances the negative log-likelihood term induced by the Gamma noise and the regularizer $\Psi(u)$, which encodes prior information on u. By using TV regularization, AA [8] proposed the following variational model for removing multiplicative Gamma noise:

$$\min_{u>0} \int_\Omega \left(\log u + \frac{f}{u} \right) dx + \mu \int_\Omega |\nabla u| \, dx, \tag{2.2}$$

where $|\nabla u| = \sqrt{(\partial_{x_1} u)^2 + (\partial_{x_2} u)^2}$ with $x = (x_1, x_2)$. The TV regularizer is well known for its convexity, edge-preserving properties, and wide applicability in image processing. However, the nonconvexity of the AA model's data-fidelity term makes the overall objective (2.2) nonconvex, which may result in convergence to local minima and sensitivity to initialization.

Shi and Osher (SO) [9] addressed the limitations of the model (2.2) by applying a logarithmic transformation $w = \log u$ while retaining the original variable, resulting in a convex variational model.

$$\min_u \lambda \int_\Omega \left(u + f e^{-u} \right) dx + \int_\Omega |\nabla u| \, dx.$$

As shown in [9], this convex model outperforms the model (2.2) and eliminates dependence on initialization. However, these models primarily target multiplicative noise and do not explicitly handle the simultaneous presence of additive Gaussian noise.

Assume the observed data follows $f = u\eta + v$, where η is multiplicative Gamma noise and $v \sim \mathcal{N}(0, \sigma^2)$. To jointly address both noise types, the authors in [23] introduced an infimal-convolution-based data-fidelity term derived from (2.1):

$$\Phi(u, f) := \inf_{v<f} \left\{ \int_\Omega \left(\log u + \frac{f-v}{u} - \frac{M-1}{M} \log(f-v) \right) dx + \frac{\lambda}{2} \int_\Omega v^2 \, dx \right\},$$

where $\lambda > 0$ is a regularization parameter that balances smoothing with fidelity to each noise component. In addition, following the SO model, a logarithmic transformation $w = \log(u)$ was applied while keeping the original variable, leading to the reformulated data-fidelity term:

$$\tilde{\Phi}(u, f) := \inf_{v<f} \left\{ \int_\Omega \Big(u + (f - v)e^{-u} - \gamma \log(f - v) \Big) dx + \frac{\lambda}{2} \int_\Omega v^2 \, dx \right\}, \tag{2.3}$$

where $\gamma = \frac{M-1}{M}$. In [23], this fidelity term was combined with SVTV to restore color images corrupted by mixed multiplicative and Gaussian noise, demonstrating its effectiveness over existing single-fidelity methods.

2.2. *Saturation-value total variation*

For a color image $\boldsymbol{u} = (\boldsymbol{u}_r, \boldsymbol{u}_g, \boldsymbol{u}_b)$, the saturation (S) and value (V) components can be expressed in terms of the RGB channels as

$$S(x) = \frac{1}{3} \|\mathbf{C}\boldsymbol{u}(x)^T\|_2, \quad V(x) = \frac{1}{\sqrt{3}} |\boldsymbol{u}_r(x) + \boldsymbol{u}_g(x) + \boldsymbol{u}_b(x)|,$$

where $x = (x_1, x_2) \in \Omega$, $\| \cdot \|_2$ is the Euclidean norm and

$$\mathbf{C} = \begin{bmatrix} 2 & -1 & -1 \\ -1 & 2 & -1 \\ -1 & -1 & 2 \end{bmatrix}, \quad \boldsymbol{u}(x)^T = \begin{bmatrix} \boldsymbol{u}_r(x) \\ \boldsymbol{u}_g(x) \\ \boldsymbol{u}_b(x) \end{bmatrix}.$$

Noting that structural features such as edges and textures are primarily captured in the saturation and value components, Jia et al. [26] introduced the SVTV regularization for color images:

$$\text{SV-TV}(\boldsymbol{u}) = \int_\Omega \sqrt{\sum_{j=1,2} |\partial_{x_j} \boldsymbol{u}(x)|_s^2} + \alpha \sqrt{\sum_{j=1,2} |\partial_{x_j} \boldsymbol{u}(x)|_v^2} \, dx, \tag{2.4}$$

where $\alpha > 0$ controls the relative weight of the value component and for $j = 1, 2$,

$$|\partial_{x_j} \boldsymbol{u}(x)|_s = \frac{1}{3} \|\mathbf{C}\partial_{x_j} \boldsymbol{u}(x)^T\|_2, \quad |\partial_{x_j} \boldsymbol{u}(x)|_v = \frac{1}{\sqrt{3}} |\partial_{x_j} \boldsymbol{u}_r(x) + \partial_{x_j} \boldsymbol{u}_g(x) + \partial_{x_j} \boldsymbol{u}_b(x)|,$$

with $\partial_{x_j} \boldsymbol{u}(x)^T = (\partial_{x_j} \boldsymbol{u}_r(x), \partial_{x_j} \boldsymbol{u}_g(x), \partial_{x_j} \boldsymbol{u}_b(x))^T$. The corresponding dual formulation is

$$\begin{aligned} \text{SV-TV}(\boldsymbol{u}) \quad := \quad \sup_{(\phi_1, \phi_2) \in \mathcal{K}^2, \phi_3 \in \mathcal{K}^1} \Big\{ \int_\Omega & \frac{1}{\sqrt{2}} (\boldsymbol{u}_r(x) - \boldsymbol{u}_g(x)) \operatorname{div}(\phi_1(x)) \\ & + \frac{1}{\sqrt{6}} (\boldsymbol{u}_r(x) + \boldsymbol{u}_g(x) - 2\boldsymbol{u}_b(x)) \operatorname{div}(\phi_2(x)) \\ & + \frac{\alpha}{\sqrt{3}} (\boldsymbol{u}_r(x) + \boldsymbol{u}_g(x) + \boldsymbol{u}_b(x)) \operatorname{div}(\phi_3(x)) \Big\} \, dx, \end{aligned} \tag{2.5}$$

where $\mathcal{K}^m = C^1(\Omega, \mathbb{B}^{2m})$ denotes the space of continuously differentiable functions with compact support in Ω that take values in the closed unit ball $\mathbb{B}^{2m} \subset \mathbb{R}^{2m}$. The convexity, lower semi-continuity, and compactness properties of SVTV were established in [26] based on this dual formulation.

From the dual formulation (2.5), the matrix $\mathbf{P}$ can be defined, which is related to $\mathbf{C}$ as follows:

$$\mathbf{P} = \begin{bmatrix} \frac{1}{\sqrt{2}} & -\frac{1}{\sqrt{2}} & 0 \\ \frac{1}{\sqrt{6}} & \frac{1}{\sqrt{6}} & -\frac{2}{\sqrt{6}} \\ \frac{1}{\sqrt{3}} & \frac{1}{\sqrt{3}} & \frac{1}{\sqrt{3}} \end{bmatrix}, \qquad \mathbf{C} = \mathbf{P}^T A \mathbf{P} \quad \text{with} \quad \mathbf{A} = \begin{bmatrix} 3 & 0 & 0 \\ 0 & 3 & 0 \\ 0 & 0 & 0 \end{bmatrix}.$$

Thus, by defining $\tilde{\boldsymbol{u}}(x) = \mathbf{P}\boldsymbol{u}(x)^T$ for $x \in \Omega$, the saturation and value components can be expressed compactly as $S(x) = \|(\tilde{\boldsymbol{u}}_1(x), \tilde{\boldsymbol{u}}_2(x))\|_2$ and $V(x) = |\tilde{\boldsymbol{u}}_3(x)|$.

2.3. Group-based sparse representation

This subsection provides a brief overview of the GSR model [39] for grayscale image restoration.

Let $\mathbf{x} \in \mathbb{R}^{N_1 \times N_2}$ denote a grayscale image. The image is first partitioned into N overlapping patches $\mathbf{x}_k$ of size $\sqrt{P} \times \sqrt{P}$ using a stride of S pixels, where $k = 1, 2, \ldots, N$. For each reference patch $\mathbf{x}_k$, the c most similar patches are identified within a local search window of size $L \times L$, and these patches are stacked column-wise to form the group matrix $\boldsymbol{x}_{\boldsymbol{G}_k} = [\boldsymbol{x}_{\boldsymbol{G}_k,1}, \boldsymbol{x}_{\boldsymbol{G}_k,2}, ..., \boldsymbol{x}_{\boldsymbol{G}_k,c}] \in \mathbb{R}^{P \times c}$. The grouping operation can be expressed via a linear operator $\boldsymbol{R}_{\boldsymbol{G}_k}$ such that $\boldsymbol{x}_{\boldsymbol{G}_k} = \boldsymbol{R}_{\boldsymbol{G}_k}(\boldsymbol{x})$. Its adjoint $\boldsymbol{R}_{\boldsymbol{G}_k}^T$ places the group back into the image domain at the corresponding patch location, padding zeros elsewhere.

The GSR model assumes that each group $\boldsymbol{x}_{\boldsymbol{G}_k}$ can be accurately represented using only a few atoms from a self-adaptive dictionary $\boldsymbol{D}_{\boldsymbol{G}_k} = [\boldsymbol{d}_{\boldsymbol{G}_k,1}, \boldsymbol{d}_{\boldsymbol{G}_k,2}, \ldots, \boldsymbol{d}_{\boldsymbol{G}_k,m}]$, which is learned during optimization. Each dictionary atom $\boldsymbol{d}_{\boldsymbol{G}_k,i} \in \mathbb{R}^{P \times c}$ has the same dimensions as the group $\boldsymbol{x}_{\boldsymbol{G}_k}$, and the number of atoms is set to $m = \min(P, c)$. The sparse coding process seeks a sparse coefficient vector $\boldsymbol{\alpha}_{\boldsymbol{G}_k} = [\alpha_{\boldsymbol{G}_k,1}, \alpha_{\boldsymbol{G}_k,2}, \ldots, \alpha_{\boldsymbol{G}_k,m}]^T$ such that $\boldsymbol{x}_{\boldsymbol{G}_k} = \boldsymbol{D}_{\boldsymbol{G}_k}\boldsymbol{\alpha}_{\boldsymbol{G}_k} := \sum_{i=1}^m \alpha_{\boldsymbol{G}_k,i}\, \boldsymbol{d}_{\boldsymbol{G}_k,i}$. After estimating the sparse codes for all groups, the image is reconstructed by aggregating all group contributions as

$$\boldsymbol{x} = \boldsymbol{D}_{\boldsymbol{G}} \circ \boldsymbol{\alpha}_{\boldsymbol{G}} := \sum_{k=1}^{N} \boldsymbol{R}_{\boldsymbol{G}_k}^T(\boldsymbol{D}_{\boldsymbol{G}_k}\boldsymbol{\alpha}_{\boldsymbol{G}_k})./\sum_{k=1}^{N} \boldsymbol{R}_{\boldsymbol{G}_k}^T(\mathbf{1}_{P\times c}), \tag{2.6}$$

where $\boldsymbol{D}_{\boldsymbol{G}}$ and $\boldsymbol{\alpha}_{\boldsymbol{G}}$ denote the concatenation of all group dictionaries and corresponding sparse codes, respectively, The symbol ./ represents element-wise division, $\mathbf{1}_{P\times c}$ is an all-ones matrix used for normalization, and $\circ$ denotes the group-based synthesis operator.

For an observed degraded image $\boldsymbol{y} = H\boldsymbol{x} + v$, where H is a known linear degradation operator and v denotes additive noise, the GSR-based restoration problem is formulated as

$$\hat{\boldsymbol{\alpha}}_{\boldsymbol{G}} := \arg\min_{\boldsymbol{\alpha}_{\boldsymbol{G}}} \frac{1}{2}\|H\boldsymbol{D}_{\boldsymbol{G}} \circ \boldsymbol{\alpha}_{\boldsymbol{G}} - \boldsymbol{y}\|_2^2 + \mu\,\|\boldsymbol{\alpha}_{\boldsymbol{G}}\|_0, \tag{2.7}$$

where $\mu > 0$ is a regularization parameter that balances data fidelity and sparsity, and $\|\boldsymbol{\alpha}_{\boldsymbol{G}}\|_0$ counts the number of nonzero elements in $\boldsymbol{\alpha}_{\boldsymbol{G}}$. With an appropriately constructed self-adaptive dictionary $\boldsymbol{D}_{\boldsymbol{G}}$, problem (2.7) can be efficiently solved via sparse approximation techniques. The restored image is then obtained via (2.6) as $\hat{\boldsymbol{x}} = \boldsymbol{D}_{\boldsymbol{G}} \circ \hat{\boldsymbol{\alpha}}_{\boldsymbol{G}}$.

3. Proposed model and algorithm

In this section, we present a variational model for denoising color images corrupted by mixed multiplicative and Gaussian noise, along with an optimization algorithm for its solution.

3.1. Proposed model

Consider a noisy color image $\boldsymbol{f}:\Omega\to\mathbb{R}^3$, degraded by a mixture of multiplicative Gamma noise and additive Gaussian noise, where $\Omega=\{1,2,...,N_1\}\times\{1,2,...,N_2\}$. The degradation model is

$$\boldsymbol{f}_s^{ch}=\boldsymbol{u}_s^{ch}\cdot\eta_s^{ch}+\boldsymbol{v}_s^{ch},\quad s\in\Omega,\quad ch=r,g,b,\tag{3.1}$$

where $\boldsymbol{u}\in\mathbb{R}^{N_1\times N_2\times 3}$ denotes the clean image, η_s^{ch} represents multiplicative Gamma noise following the distribution in (1.1), and $\boldsymbol{v}_s^{ch}\sim\mathcal{N}(0,\sigma^2)$ represents additive Gaussian noise.

The degradation model in (3.1) gives rise to an ill-posed inverse problem; thus, we formulate a variational minimization problem to recover $\boldsymbol{u}$ from the observed data $\boldsymbol{f}$. To simultaneously address multiplicative Gamma noise and additive Gaussian noise, we introduce the logarithmic variable $\boldsymbol{w}=\log(\boldsymbol{u})$, while keeping $\boldsymbol{u}$ as the primary variable, and employ the data-fidelity term in (2.3):

$$F(\boldsymbol{u},\boldsymbol{v})=\left\langle\boldsymbol{u}+(\boldsymbol{f}-\boldsymbol{v})e^{-\boldsymbol{u}}-\gamma\log(\boldsymbol{f}-\boldsymbol{v}),\ \mathbf{1}\right\rangle+\frac{\lambda}{2}\|\boldsymbol{v}\|_2^2,\tag{3.2}$$

where $\boldsymbol{v}<\boldsymbol{f}$, $\gamma=\frac{M-1}{M}$, $\langle\cdot,\cdot\rangle$ denotes the inner product, $\mathbf{1}\in\mathbb{R}^{N_1\times N_2\times 3}$, and $\lambda>0$ regulates the penalty on the Gaussian noise component. The quadratic term $\frac{\lambda}{2}\|\boldsymbol{v}\|_2^2$ models and extracts the additive Gaussian noise from $\boldsymbol{f}$, while the remaining terms correspond to the data-fidelity for the multiplicative Gamma noise applied to $\boldsymbol{f}-\boldsymbol{v}$. This unified formulation decouples the two noise components, enabling effective restoration of color images corrupted by mixed noise.

We first combine the data-fidelity term (3.2) with SVTV regularization, yielding the model in [23]. SVTV effectively suppresses noise in homogeneous regions and preserves edges, while substantially reducing color artifacts compared with conventional TV. However, its reliance on local derivatives limits the preservation of fine textures and details, and its first-order formulation may produce staircase artifacts. To overcome these limitations, we incorporate GSR as an additional regularization term. By representing the image as $\boldsymbol{u}=\boldsymbol{D_G}\circ\boldsymbol{\alpha_G}$, we formulate the minimization problem as

$$\min_{\boldsymbol{u},\boldsymbol{\alpha_G},\boldsymbol{v}<\boldsymbol{f}}\ E(\boldsymbol{u},\boldsymbol{\alpha_G},\boldsymbol{v})=F(\boldsymbol{u},\boldsymbol{v})+\mu\|\boldsymbol{\alpha_G}\|_0+\beta\,\text{SV-TV}(\boldsymbol{u}),\quad\text{subject to:}\quad\boldsymbol{u}=\boldsymbol{D_G}\circ\boldsymbol{\alpha_G},\tag{3.3}$$

where $\mu>0$ is a regularization parameter that promotes sparsity in the coefficients α_G, $\beta>0$ controls the smoothness of $\boldsymbol{u}$, and SV-TV($\boldsymbol{u}$) is defined in (2.4). After solving the problem (3.3), the restored image is obtained as $e^{\boldsymbol{u}}$. This model extends [23] by incorporating the GSR framework and builds upon [15], which combined SVTV and GSR for heavy multiplicative noise removal. However, the model in [15] was designed specifically for multiplicative noise and cannot effectively handle additive Gaussian noise. In that work, SVTV played only a minor role, primarily reducing slight ringing or block artifacts from patch-based processing. From a regularization perspective, GSR imposes a sparsity-based nonlocal prior that promotes low-dimensional structure within groups of similar patches, encouraging strong correlations among them. This property makes GSR particularly effective at preserving repeated or correlated patterns, including fine textures (e.g., grass, fabric weaves), periodic or geometric structures (e.g., tiles, fences, lattice patterns), and directional features. Unlike first-order local regularizers, which often oversmooth high-frequency details, GSR retains consistent variations across similar patches. The performance of GSR, however, depends on accurate patch grouping. In smooth regions or under heavy mixed noise, distortions may impair patch similarity estimation, leading to inaccurate grouping and residual artifacts. Moreover, without complementary local regularization, GSR may be less effective near sharp edges, where patch matching across intensity discontinuities becomes unreliable. SVTV complements GSR by providing local edge-preserving regularization in the saturation-value domain. It promotes piecewise smoothness, suppresses color artifacts in homogeneous regions, and stabilizes reconstruction around edges. While SVTV effectively handles smooth areas, GSR preserves nonlocal textures and repeated patterns that SVTV alone may oversmooth. By combining SVTV and GSR, the proposed model integrates a local edge-preserving prior with a nonlocal sparsity-based structural prior, forming a principled framework that balances texture preservation and mixed-noise suppression. This complementary interaction demonstrates that the model is not merely an empirical combination of priors but a coherent fusion of local and nonlocal regularization mechanisms tailored for mixed-noise removal in color images.

For GSR, we adopt the approach in [15], which evaluates patch similarity using full-color patches across all channels, thereby capturing inter-channel relationships more effectively. Unlike methods that process each color channel independently, the full-color GSR framework models all RGB channels simultaneously, exploiting their inherent correlations. This integrated representation preserves structures such as edges, textures, and fine details consistently across channels, reducing color mismatches and artifacts that commonly arise from channel-wise processing. Specifically, for a color patch $\boldsymbol{u}_k = [\boldsymbol{u}_k^r, \boldsymbol{u}_k^g, \boldsymbol{u}_k^b]^T \in \mathbb{R}^{3P}$, where $\boldsymbol{u}_k^{ch}$ denotes a $\sqrt{P} \times \sqrt{P}$ patch in the ch-channel ($ch = r, g, b$), the group $\boldsymbol{u}_{\boldsymbol{G}_k}$ of the c most similar patches is reconstructed as

$$\boldsymbol{u}_{\boldsymbol{G}_k} = \begin{bmatrix} \boldsymbol{u}^r_{\boldsymbol{G}_{k,1}} & \boldsymbol{u}^r_{\boldsymbol{G}_{k,2}} & \cdots & \boldsymbol{u}^r_{\boldsymbol{G}_{k,c}} \\ \boldsymbol{u}^g_{\boldsymbol{G}_{k,1}} & \boldsymbol{u}^g_{\boldsymbol{G}_{k,2}} & \cdots & \boldsymbol{u}^g_{\boldsymbol{G}_{k,c}} \\ \boldsymbol{u}^b_{\boldsymbol{G}_{k,1}} & \boldsymbol{u}^b_{\boldsymbol{G}_{k,2}} & \cdots & \boldsymbol{u}^b_{\boldsymbol{G}_{k,c}} \end{bmatrix} \in \mathbb{R}^{3P \times c}.$$

To identify similar patches in $\boldsymbol{u}$, we consider the following model, obtained by applying a logarithmic transformation to (3.1): $\hat{\boldsymbol{f}} = \boldsymbol{u} + \hat{\eta}$, where $\hat{\boldsymbol{f}} = \log(\boldsymbol{f} - \boldsymbol{v})$, $\boldsymbol{u}$ denotes the logarithmically transformed clean image, and $\hat{\eta} = \log(\eta)$. This formulation assumes that $\boldsymbol{v}$ effectively removes the additive Gaussian noise component, leaving primarily multiplicative noise. Under this assumption, the logarithmic transformation converts multiplicative noise into an approximately additive form, which is easier to handle statistically. As illustrated in Figure 1, the histograms of $\hat{\eta}$ in the RGB color space closely resemble Gaussian distributions across all noise levels. Motivated by this observation, we extract color patches in the RGB space and measure the similarity between two patches, $\boldsymbol{u}_{k_1}$ and $\boldsymbol{u}_{k_2}$, using the Euclidean distance. Although $\boldsymbol{v}$ is estimated iteratively and may be imprecise in early iterations, the log-domain noise approaches a Gaussian distribution as the estimation converges. Consequently, Euclidean distance provides a reasonable and practical metric for patch similarity throughout the iterative process.

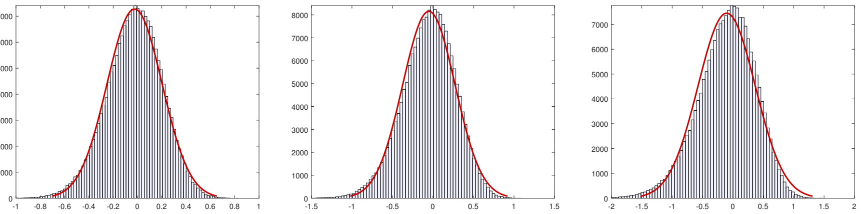

(a) $M = 20$ (b) $M = 10$ (c) $M = 5$

Figure 1. Histogram of $\hat{\eta} = \log(\eta)$ with fitted normal density curves (red) at noise levels $M = 20, 10, 5$.

Parameter roles and selection. The parameters λ, μ, and β play complementary roles in balancing data fidelity, texture modeling, and spatial regularity. From a MAP perspective, the balance parameter λ in the infimal convolution data-fidelity term corresponds to the precision of the Gaussian noise component $\boldsymbol{v}$. Since $\boldsymbol{v}$ models Gaussian noise with variance σ^2, its negative log-likelihood yields a quadratic term weighted by $1/\sigma^2$. Thus, λ should scale inversely with σ^2: higher Gaussian noise favors smaller λ, relaxing the penalty on $\boldsymbol{v}$, while lower noise favors larger λ, enforcing stricter fidelity. The sparsity weight μ, which controls the group-sparse representation, can be made adaptive [46]. For each patch group $\boldsymbol{u}_{\boldsymbol{G}_k}$, μ is inversely related to the local patch variance $\sigma^2_{G_k}$, so that smoother regions receive stronger sparsity while textured regions preserve details. In the mixed-noise setting, μ also depends on both the multiplicative noise level M and the Gaussian variance σ^2. Stronger noise in either component increases patch distortions, requiring larger μ to suppress noise-induced coefficients. Conceptually, this can be expressed as $\mu_{G_k} \propto \frac{g(M,\sigma)}{\sigma_{G_k}+\epsilon}$, where $g(M, \sigma)$ grows with overall noise strength and ϵ prevents division by zero. This formulation allows μ to adapt both to local patch smoothness and to the global noise level, effectively targeting nonlocal correlations in similar patches. For simplicity and reproducibility, fixed μ values were manually selected for each image and noise setting, as detailed in the experimental section. The SVTV weight β governs local smoothness in the saturation-value domain. Larger β suppresses noise more effectively in homogeneous regions but may oversmooth fine textures and edges. In practice, β typically increases with the overall noise level: smaller M corresponds to stronger multiplicative fluctuations, while larger σ^2 introduces larger Gaussian perturbations. By adjusting β according to the noise characteristics, the model balances noise suppression with detail preservation. While the multiplicative Gamma noise level M does not yield a direct analytical formula for the regularization terms, its effect is implicitly handled through the joint adjustment of λ, μ, and β. In combination, μ and β complement each other: μ preserves nonlocal textures via the GSR prior, whereas β stabilizes local smoothness via SVTV. These considerations offer qualitative, model-consistent guidance for parameter selection and justify the empirical choices reported in the experimental section.

3.2. Optimization algorithm

First, the proposed model (3.3) can be equivalently rewritten as

$$\min_{\boldsymbol{u},\boldsymbol{\alpha}_{\boldsymbol{G}},\boldsymbol{v}} \mathcal{E}(\boldsymbol{u}, \boldsymbol{\alpha}_{\boldsymbol{G}}, \boldsymbol{v}) = E(\boldsymbol{u}, \boldsymbol{\alpha}_{\boldsymbol{G}}, \boldsymbol{v}) + \iota_{C_1}(\boldsymbol{u}, \boldsymbol{\alpha}_{\boldsymbol{G}}) + \iota_{C_2}(\boldsymbol{v}), \tag{3.4}$$

where $C_1 = \{(\boldsymbol{u}, \boldsymbol{\alpha}_{\boldsymbol{G}}) : \boldsymbol{u} = \boldsymbol{D}_{\boldsymbol{G}} \circ \boldsymbol{\alpha}_{\boldsymbol{G}}\}$, $C_2 = \{\boldsymbol{v} : \boldsymbol{v} < \boldsymbol{f}\}$, and $\iota_C(z)$ is the indicator function of a set C, defined by $\iota_C(z) = 0$ if $z \in C$ and ∞ otherwise. Here, $\boldsymbol{D}_{\boldsymbol{G}}$ is not an optimization variable; it is deterministically computed (via SVD) from the current iterate and does not depend on α_G. Therefore, it does not need to be included explicitly in the optimization, and the problem can be solved over $(\boldsymbol{u}, \boldsymbol{\alpha}_{\boldsymbol{G}}, \boldsymbol{v})$ only.

The optimization problem in (3.4) is nonconvex and nonsmooth due to the presence of both ℓ_0 and ℓ_1 regularization terms, and the variables $\boldsymbol{u}$ and $\boldsymbol{v}$ are coupled through the data-fidelity term, which complicates direct joint optimization. To handle this coupling, we adopt a block-coordinate approach. Specifically, the classical alternating minimization algorithm (AMA) [53] iteratively updates one block of variables while keeping the others fixed, decomposing the original problem into two tractable subproblems. Although the AMA is attractive for its simplicity, it generally lacks strong convergence guarantees in nonconvex and nonsmooth settings. To address these limitations, we employ the proximal AMA (PAMA) [54], which augments each subproblem with proximal regularization terms. Accordingly, at iteration n, we alternate between solving the following two subproblems:

$$\begin{aligned} \boldsymbol{v}^{n+1} &:= \arg\min_{\boldsymbol{v}} \left\{ E(\boldsymbol{u}^n, \boldsymbol{\alpha}_{\boldsymbol{G}}^n, \boldsymbol{v}) + \iota_{C_2}(\boldsymbol{v}) + \frac{\delta}{2}\|\boldsymbol{v} - \boldsymbol{v}^n\|_2^2 \right\}, \\ (\boldsymbol{u}^{n+1}, \boldsymbol{\alpha}_{\boldsymbol{G}}^{n+1}) &:= \arg\min_{\boldsymbol{u}, \boldsymbol{\alpha}_{\boldsymbol{G}}} \left\{ E(\boldsymbol{u}, \boldsymbol{\alpha}_{\boldsymbol{G}}, \boldsymbol{v}^{n+1}) + \iota_{C_1}(\boldsymbol{u}, \boldsymbol{\alpha}_{\boldsymbol{G}}) + \frac{\delta}{2}\|\boldsymbol{u} - \boldsymbol{u}^n\|_2^2 + \frac{\delta}{2}\|\boldsymbol{\alpha}_{\boldsymbol{G}} - \boldsymbol{\alpha}_{\boldsymbol{G}}^n\|_2^2 \right\}, \end{aligned} \tag{3.5}$$

where $\delta > 0$ is a proximal parameter. The proximal terms stabilize the iterations and ensure sufficient descent of the objective, which is critical for convergence in nonconvex and nonsmooth settings.

To establish the convergence of the proposed PAMA in (3.5), we first show that the iterates remain bounded under a mild assumption, as stated in the following lemma.

Lemma 3.1. *Assume that* $\inf_{\boldsymbol{v}\in C_2}(\boldsymbol{f} - \boldsymbol{v}) > 0$*. Then the sequence* $\{(\boldsymbol{u}^n, \boldsymbol{\alpha}_{\boldsymbol{G}}^n, \boldsymbol{v}^n)\}$ *generated by the PAMA in* (3.5) *is bounded.*

Proof. First, note that the energy $\mathcal{E}$ is proper: it is finite at least at the initial iterate $(\boldsymbol{u}^0, \boldsymbol{\alpha}_{\boldsymbol{G}}^0, \boldsymbol{v}^0)$ and never takes the value $-\infty$. Hence, the PAMA iterates are well-defined, and the descent inequalities below are meaningful.

By construction of the PAMA, the iterates satisfy

$$\begin{aligned} \mathcal{E}(\boldsymbol{u}^n, \boldsymbol{\alpha}_{\boldsymbol{G}}^n, \boldsymbol{v}^{n+1}) + \frac{\delta}{2}\|\boldsymbol{v}^{n+1} - \boldsymbol{v}^n\|_2^2 &\leq \mathcal{E}(\boldsymbol{u}^n, \boldsymbol{\alpha}_{\boldsymbol{G}}^n, \boldsymbol{v}^n), \\ \mathcal{E}(\boldsymbol{u}^{n+1}, \boldsymbol{\alpha}_{\boldsymbol{G}}^{n+1}, \boldsymbol{v}^{n+1}) + \frac{\delta}{2}\|\boldsymbol{u}^{n+1} - \boldsymbol{u}^n\|_2^2 + \frac{\delta}{2}\|\boldsymbol{\alpha}_{\boldsymbol{G}}^{n+1} - \boldsymbol{\alpha}_{\boldsymbol{G}}^n\|_2^2 &\leq \mathcal{E}(\boldsymbol{u}^n, \boldsymbol{\alpha}_{\boldsymbol{G}}^n, \boldsymbol{v}^{n+1}). \end{aligned}$$

Adding these inequalities gives the monotone decrease of the augmented energy.

$$\mathcal{E}(\boldsymbol{u}^{n+1}, \boldsymbol{\alpha}_{\boldsymbol{G}}^{n+1}, \boldsymbol{v}^{n+1}) + \frac{\delta}{2}\|\boldsymbol{u}^{n+1} - \boldsymbol{u}^n\|_2^2 + \frac{\delta}{2}\|\boldsymbol{\alpha}_{\boldsymbol{G}}^{n+1} - \boldsymbol{\alpha}_{\boldsymbol{G}}^n\|_2^2 + \frac{\delta}{2}\|\boldsymbol{v}^{n+1} - \boldsymbol{v}^n\|_2^2 \leq \mathcal{E}(\boldsymbol{u}^n, \boldsymbol{\alpha}_{\boldsymbol{G}}^n, \boldsymbol{v}^n). \tag{3.6}$$

Next, let $(\boldsymbol{u}, \boldsymbol{v})$ belong to the domain $\{(\boldsymbol{u}, \boldsymbol{v}) : \boldsymbol{v} < \boldsymbol{f}\}$. By the assumption $\inf_{\boldsymbol{v}\in C_2}(\boldsymbol{f} - \boldsymbol{v}) > 0$, there exists a constant $\epsilon > 0$ such that $(\boldsymbol{f}_s - \boldsymbol{v}_s) \geq \epsilon$ for all $s \in \Omega$. For each pixel $s \in \Omega$, define

$$\phi(\boldsymbol{u}_s, \boldsymbol{v}_s) = \boldsymbol{u}_s + (\boldsymbol{f}_s - \boldsymbol{v}_s)e^{-\boldsymbol{u}_s} - \gamma \log(\boldsymbol{f}_s - \boldsymbol{v}_s). \tag{3.7}$$

Since $\boldsymbol{f}_s - \boldsymbol{v}_s \geq \epsilon$, the logarithmic term is bounded from below. Moreover, $\phi(\boldsymbol{u}_s, \boldsymbol{v}_s) \to +\infty$ as $\boldsymbol{u}_s \to +\infty$ due to the linear term, and $\phi(\boldsymbol{u}_s, \boldsymbol{v}_s) \to +\infty$ as $\boldsymbol{u}_s \to -\infty$ due to the exponential term. Hence, $\phi(\boldsymbol{u}_s, \boldsymbol{v}_s)$ is bounded below on $\mathbb{R}$ for each $s \in \Omega$. Summing over all pixels yields the existence of a constant $C > -\infty$ such that $\sum_{s\in\Omega} \phi(\boldsymbol{u}_s, \boldsymbol{v}_s) \geq C$. In addition, the quadratic term $\frac{\lambda}{2}\|\boldsymbol{v}\|_2^2$ is nonnegative. Therefore, the fidelity term $F(\boldsymbol{u}, \boldsymbol{v})$ admits a finite lower bound on the feasible set. The constraint $\boldsymbol{u} = \boldsymbol{D}_{\boldsymbol{G}} \circ \boldsymbol{\alpha}_{\boldsymbol{G}}$ restricts $\boldsymbol{u}$ to lie in the image of the linear operator $\boldsymbol{D}_{\boldsymbol{G}}$, which is a subset of $\mathbb{R}^{N_1\times N_2\times 3}$. Since $F(\boldsymbol{u}, \boldsymbol{v})$ is already bounded below for all $\boldsymbol{u}$ and $\boldsymbol{v} < \boldsymbol{f}$, this restriction cannot introduce new directions along which the fidelity term decreases without bound. Furthermore, the ℓ_0 regularization term $\|\boldsymbol{\alpha}_{\boldsymbol{G}}\|_0$ is nonnegative and therefore does not contribute any negative unbounded directions in the coefficient space. Moreover, the regularization term SV-TV($\boldsymbol{u}$) is nonnegative, and the indicator functions ι_{C_1} and ι_{C_2} vanish on feasible iterates. Consequently, the total energy $\mathcal{E}(\boldsymbol{u}, \boldsymbol{\alpha}_{\boldsymbol{G}}, \boldsymbol{v})$ is bounded below by a finite constant. Since the PAMA scheme generates a monotone decreasing sequence of energy values, it follows that the sequence $\{\mathcal{E}(\boldsymbol{u}^n, \boldsymbol{\alpha}_{\boldsymbol{G}}^n, \boldsymbol{v}^n)\}$ converges.

Suppose, for contradiction, that the sequence is unbounded, so that at least one of $\|\boldsymbol{u}^n\|_2$, $\|\boldsymbol{\alpha}_{\boldsymbol{G}}^n\|_2$, or $\|\boldsymbol{v}^n\|_2$ diverges. The proximal terms

$$\frac{\delta}{2}\|\boldsymbol{u}^{n+1} - \boldsymbol{u}^n\|_2^2, \quad \frac{\delta}{2}\|\boldsymbol{\alpha}_{\boldsymbol{G}}^{n+1} - \boldsymbol{\alpha}_{\boldsymbol{G}}^n\|_2^2, \quad \frac{\delta}{2}\|\boldsymbol{v}^{n+1} - \boldsymbol{v}^n\|_2^2$$

grow quadratically with the iterate differences and will thus make the left-hand side of (3.6) arbitrarily large, contradicting the convergence of the sequence $\{\mathcal{E}(\boldsymbol{u}^n, \boldsymbol{\alpha}_{\boldsymbol{G}}^n, \boldsymbol{v}^n)\}$. Hence, no component of $\{(\boldsymbol{u}^n, \boldsymbol{\alpha}_{\boldsymbol{G}}^n, \boldsymbol{v}^n)\}$ can diverge, and the sequence is bounded. □

Next, we prove the convergence of the PAMA iterates generated by (3.5), adopting the analysis framework developed in [54]. We first recall the definitions of semi-algebraic and subanalytic sets and functions from [55] and [56].

Definition 3.1. *(Semi-algebraic and subanalytic functions)*

(i) A subset $A \subset \mathbb{R}^d$ is called a semi-algebraic set if there exists a finite number of real polynomial functions P_{ij}, $Q_{ij} : \mathbb{R}^d \to \mathbb{R}$ such that $A = \bigcup_{j=1}^{p} \bigcap_{i=1}^{q} \{x \in \mathbb{R}^d : P_{ij}(x) = 0, \; Q_{ij}(x) < 0\}$. A function $g : \mathbb{R}^d \to (-\infty, +\infty]$ is called semi-algebraic if its graph $\{(x,t) \in \mathbb{R}^{d+1} : g(x) = t\}$ is a semi-algebraic subset in $\mathbb{R}^{d+1}$.

(ii) A function $g : \mathbb{R}^d \to (-\infty, +\infty]$ is called subanalytic if its graph is a subanalytic subset of $\mathbb{R}^{d+1}$; equivalently, locally it is the projection of a bounded semianalytic set.

All semi-algebraic and real-analytic functions are subanalytic. Moreover, finite sums, compositions, and products of subanalytic functions remain subanalytic. Every proper, lower semicontinuous, subanalytic function satisfies the Kurdyka–Łojasiewicz (KL) property [57], which is crucial for establishing convergence of the PAMA iterates.

Theorem 3.1. *Assume that* $\inf_{\boldsymbol{v}\in C_2}(\boldsymbol{f} - \boldsymbol{v}) > 0$. *Then the sequence* $\{(\boldsymbol{u}^n, \boldsymbol{\alpha}_{\boldsymbol{G}}^n, \boldsymbol{v}^n)\}$ *generated by the PAMA in* (3.5) *converges to a critical point of* $\mathcal{E}(\boldsymbol{u}, \boldsymbol{\alpha}_{\boldsymbol{G}}, \boldsymbol{v})$ *defined in* (3.4).

Proof. Based on Theorem 9 in [54], it is sufficient to show that the following conditions hold:

(1) The objective function $\mathcal{E}(\boldsymbol{u}, \boldsymbol{\alpha}_{\boldsymbol{G}}, \boldsymbol{v})$ in (3.4) is a KL function.

(2) $\nabla F(\boldsymbol{u}, \boldsymbol{v})$ is Lipschitz continuous on any bounded subset of its domain.

First, we prove the first condition as follows:

- Each pixelwise component defined in (3.7) is real-analytic on the domain $\{\boldsymbol{v}_s < \boldsymbol{f}_s\}$, since it is composed of linear, exponential, and logarithmic functions, all of which are real-analytic. The sum of real-analytic functions is real-analytic, and every real-analytic function is subanalytic. The full fidelity term $F(\boldsymbol{u}, \boldsymbol{v}) = \sum_{s\in\Omega} \phi(\boldsymbol{u}_s, \boldsymbol{v}_s) + \frac{\lambda}{2}\|\boldsymbol{v}\|_2^2$ is a finite sum of subanalytic functions (note that the quadratic term $\frac{\lambda}{2}\|\boldsymbol{v}\|_2^2$ is also real-analytic and hence subanalytic). Therefore, F is subanalytic. Since F is proper and lower semicontinuous, it satisfies the KL property.
- The synthesis constraint $\boldsymbol{u} = \boldsymbol{D_G} \circ \alpha_G$ defines the set C_1. Since $\boldsymbol{D_G}$ is linear, C_1 is an affine subspace. Affine subspaces are defined by linear equalities, which are polynomial equations, so C_1 is a semi-algebraic set. Its indicator function ι_{C_1} is thus semi-algebraic. Moreover, since affine subspaces are closed sets, ι_{C_1} is lower semicontinuous. Combining these properties, ι_{C_1} satisfies the KL property.

- The set $C_2 = \{\boldsymbol{v} : \boldsymbol{v}_s < \boldsymbol{f}_s, \ \forall s \in \Omega\}$ is defined by linear inequalities. Hence, C_2 is semi-algebraic and its indictor function ι_{C_2} is semi-algebraic. Although C_2 is open and ι_{C_2} is not lower semicontinuous at the boundary, the KL property holds at all points in its domain. Under the assumption $\inf_{\boldsymbol{v}\in C_2}(\boldsymbol{f} - \boldsymbol{v}) > 0$, all iterates $\boldsymbol{v}^n$ remain strictly inside C_2, so the KL property applies along the sequence of iterates.
- Let $G(z) = \|z\|_0$ for $z \in \mathbb{R}^d$, where $d = m \times N$. The graph of G can be expressed as $\operatorname{graph}(G) = \{(z, r) \in \mathbb{R}^{d+1} : \|z\|_0 = r\} = \bigcup_{J\subseteq\{1,\dots,d\}} S_J$, where

  $$S_J = \{(z, r) : r = |J|, \ \ z_i \neq 0 \ \text{ if } \ i \in J, \ \ z_i = 0 \ \text{ if } \ i \notin J\}.$$

  Equivalently, the condition $z_i \neq 0$ can be written as $z_i^2 > 0$, which is a polynomial inequality. Since each S_J is defined by finitely many polynomial equalities and inequalities, it is semi-algebraic. Therefore, $\operatorname{graph}(G)$ is a finite union of semi-algebraic sets, and hence G is semi-algebraic. Furthermore, all sublevel sets

  $$\{z \in \mathbb{R}^d : \|z\|_0 \le r\} = \cup_{J\subseteq\{1,\dots,d\},|J|\le r}\{z_i = 0 \ \text{ if } \ i \notin J\}$$

  are finite unions of closed linear subspaces and hence closed. Therefore, G is lower semicontinuous, thus it satisfies the KL property.
- The SVTV integrand is constructed using linear operations, including spatial derivatives and linear combinations of the color channels, together with Euclidean norms, absolute values, finite summations, and square roots of nonnegative expressions. All these operations are semi-algebraic, and therefore the SVTV pointwise integrand is a semi-algebraic function. In the discrete image setting, spatial derivatives are replaced by finite differences, and the integral over Ω reduces to a finite sum, which preserves semi-algebraicity. Moreover, the resulting SVTV functional is proper and lower semicontinuous, since it is a finite sum of continuous nonnegative terms. Consequently, the discrete SVTV functional satisfies the KL property.

Therefore, the total energy $\mathcal{E}(\boldsymbol{u}, \boldsymbol{\alpha_G}, \boldsymbol{v})$ is a finite sum of KL functions and hence satisfies the KL property.

Next, let T be a bounded subset of the domain $\{(\boldsymbol{u}, \boldsymbol{v}) : \boldsymbol{v} < \boldsymbol{f}\} \subset \mathbb{R}^d \times \mathbb{R}^d$, where $d = N_1 \times N_2 \times 3$. By the assumption, there exist constants $U > 0$ and $\epsilon > 0$ such that $|\boldsymbol{u}_s| \le U$, $\boldsymbol{f}_s - \boldsymbol{v}_s \ge \epsilon$ for all $(\boldsymbol{u}, \boldsymbol{v}) \in T$, $s \in \Omega$. The gradient of F is given pixelwise, and its Hessian is block-diagonal with 2×2 blocks:

$$\begin{aligned}
(\nabla F)_s &= \Big[\big(\nabla_{\boldsymbol{u}} F\big)_s, \big(\nabla_{\boldsymbol{v}} F\big)_s\Big]^T = \Big[1 - (\boldsymbol{f}_s - \boldsymbol{v}_s)e^{-\boldsymbol{u}_s}, -e^{-\boldsymbol{u}_s} + \gamma(\boldsymbol{f}_s - \boldsymbol{v}_s)^{-1} + \lambda \boldsymbol{v}_s\Big]^T, \\
H_s &= \begin{bmatrix} \left(\frac{\partial^2 F}{\partial u^2}\right)_s & \left(\frac{\partial^2 F}{\partial u \partial v}\right)_s \\ \left(\frac{\partial^2 F}{\partial u \partial v}\right)_s & \left(\frac{\partial^2 F}{\partial v^2}\right)_s \end{bmatrix} = \begin{bmatrix} (\boldsymbol{f}_s - \boldsymbol{v}_s)e^{-\boldsymbol{u}_s} & -e^{-\boldsymbol{u}_s} \\ -e^{-\boldsymbol{u}_s} & \gamma(\boldsymbol{f}_s - \boldsymbol{v}_s)^{-2} + \lambda \end{bmatrix}.
\end{aligned}$$

Since T is bounded, the spectral norm of H_s is bounded by

$$\|H_s\|_2 \le |b| + \max\{a, c\} = e^U + \max\left\{(\boldsymbol{f}_{\max} - \boldsymbol{v}_{\min})e^U, \gamma/\epsilon^2 + \lambda\right\} := \tilde{L},$$

where $a = (\boldsymbol{f}_s - \boldsymbol{v}_s)e^{-\boldsymbol{u}_s}$, $b = -e^{-\boldsymbol{u}_s}$, and $c = \gamma(\boldsymbol{f}_s - \boldsymbol{v}_s)^{-2} + \lambda$. Since $\nabla^2 F$ is block-diagonal, its spectral norm is the maximum over pixels:

$$\|\nabla^2 F(\boldsymbol{u}, \boldsymbol{v})\|_2 = \max_{s\in\Omega} \|H_s\|_2 \le \tilde{L}.$$

By standard results for twice continuously differentiable functions, this implies that the gradient of F is Lipschitz continuous on T with constant $\tilde{L}$; that is, for any $(\boldsymbol{u}_1, \boldsymbol{v}_1)$, $(\boldsymbol{u}_2, \boldsymbol{v}_2) \in T$,

$$\|\nabla F(\boldsymbol{u}_1, \boldsymbol{v}_1) - \nabla F(\boldsymbol{u}_2, \boldsymbol{v}_2)\|_2 \leq \tilde{L}\|(\boldsymbol{u}_1, \boldsymbol{v}_1) - (\boldsymbol{u}_2, \boldsymbol{v}_2)\|_2.$$

Therefore, the assumptions required in Theorem 9 of [54] are fulfilled, which yields the conclusion of the theorem. □

Remark 1. *The assumption in Lemma 3.1 and Theorem 3.1,* $\inf_{\boldsymbol{v}\in C_2}(\boldsymbol{f} - \boldsymbol{v}) > 0$*, requires that* $\boldsymbol{f} - \boldsymbol{v}$ *remains strictly positive. This condition is typically satisfied in practical applications because the feasible set* $C_2 = \{\boldsymbol{v} : \boldsymbol{v} < \boldsymbol{f}\}$ *explicitly enforces an upper bound on the Gaussian noise component* $\boldsymbol{v}$ *relative to the signal* $\boldsymbol{f}$*. In real imaging scenarios, the noise* $\boldsymbol{v}$ *is typically smaller in magnitude than the underlying signal* $\boldsymbol{f}$*, and the strict positivity is further maintained by the closed-form update* (3.10)*, which preserves the inequality at each iteration. Thus, the assumption is mild, physically meaningful, and naturally satisfied in practical imaging scenarios, thereby supporting the validity of the convergence analysis.*

In the following subsections, we solve the subproblems of (3.5).

3.2.1. Solving for $\boldsymbol{v}$-subproblem in (3.5)

First, we consider the $\boldsymbol{v}$-subproblem in (3.5), which can be expressed as

$$\min_{\boldsymbol{v}<\boldsymbol{f}} \left\langle (\boldsymbol{f} - \boldsymbol{v})e^{-\boldsymbol{u}^n} - \gamma \log(\boldsymbol{f} - \boldsymbol{v}),\ \mathbf{1} \right\rangle + \frac{\lambda}{2}\|\boldsymbol{v}\|_2^2 + \frac{\delta}{2}\|\boldsymbol{v} - \boldsymbol{v}^n\|_2^2. \tag{3.8}$$

Following the arguments in [23], we can show that the subproblem in (3.8) is strictly convex, and therefore admits a unique minimizer. The explicit form of the solution is summarized in the following proposition.

Proposition 3.1. *For any* $\bar{f}$, $\bar{u}$, $v_0 \in \mathbb{R}$ *and positive parameters* γ, λ, *and* δ, *define the function* $g : X \to \mathbb{R}$, *where* $X = \{v \in \mathbb{R} : v < \bar{f}\}$, *by*

$$g(v) = (\bar{f} - v)e^{-\bar{u}} - \gamma \log(\bar{f} - v) + \frac{\lambda}{2}v^2 + \frac{\delta}{2}(v - v_0)^2.$$

Then the minimization problem $\min_{v\in X} g(v)$ *admits a unique solution, which can be expressed in closed form.*

Proof. The first- and second-order derivatives of g are

$$g'(v) = -e^{-\bar{u}} + \frac{\gamma}{\bar{f} - v} + \lambda v + \delta(v - v_0), \quad g''(s) = \frac{\gamma}{(\bar{f} - v)^2} + \lambda + \delta.$$

Since all parameters are positive and $v < \bar{f}$, $g''(v) > 0$ for all $v \in X$, which implies that g is strictly convex on X. Thus, if the equation $g'(v) = 0$ has a solution, then that solution is unique. The equation $g'(v) = 0$ yields the following quadratic equation for v: $av^2 - (a\bar{f} + b)v + (b\bar{f} - \gamma) = 0$, where $a = \lambda + \delta$ and $b = e^{-\bar{u}} + \delta v_0$. The determinant $D = (a\bar{f} + b)^2 - 4a(b\bar{f} - \gamma) = (a\bar{f} - b)^2 + 4a\gamma > 0$, so the quadratic equation admits two distinct real roots. The smaller root is given by

$$\tilde{v} = \frac{(a\bar{f} + b) - \sqrt{(a\bar{f} - b)^2 + 4a\gamma}}{2a}, \tag{3.9}$$

which satisfies the condition $\tilde{v} < \bar{f}$; if $a\bar{f} - b < 0$, then

$$\tilde{v} = \frac{(a\bar{f} + b) - \sqrt{(a\bar{f} - b)^2 + 4a\gamma}}{2a} < \frac{(a\bar{f} + b) - |a\bar{f} - b|}{2a} = \bar{f},$$

while if $a\bar{f} - b \geq 0$, then

$$\tilde{v} = \frac{(a\bar{f} + b) - \sqrt{(a\bar{f} - b)^2 + 4a\gamma}}{2a} < \frac{a\bar{f} + b - (a\bar{f} - b)}{2a} = \frac{b}{a} \leq \bar{f}.$$

Therefore, $\tilde{v}$ is the unique global minimizer of the problem $\min_{v \in X} g(v)$. □

Based on the closed-form expression in (3.9), the solution $\boldsymbol{v}^{n+1}$ of problem (3.8) is given by

$$\boldsymbol{v}^{n+1} = \frac{(\lambda + \delta)\boldsymbol{f} + \exp(-\boldsymbol{u}^n) + \delta \boldsymbol{v}^n - \sqrt{((\lambda + \delta)\boldsymbol{f} - (\exp(-\boldsymbol{u}^n) + \delta \boldsymbol{v}^n))^2 + 4(\lambda + \delta)\gamma}}{2(\lambda + \delta)}. \tag{3.10}$$

3.2.2. Solving for $(\boldsymbol{u}, \boldsymbol{\alpha_G})$-subproblem in (3.5)

Now, we solve the $(\boldsymbol{u}, \boldsymbol{\alpha_G})$-subproblem in (3.5), which can be rewritten as

$$\min_{\boldsymbol{u}, \boldsymbol{\alpha_G}} \left\{ E(\boldsymbol{u}, \boldsymbol{\alpha_G}, \boldsymbol{v}^{n+1}) + \frac{\delta}{2}\|\boldsymbol{u} - \boldsymbol{u}^n\|_2^2 + \frac{\delta}{2}\|\boldsymbol{\alpha_G} - \boldsymbol{\alpha_G^n}\|_2^2 \right\}, \quad \text{subject to:} \quad \boldsymbol{u} = \boldsymbol{D_G} \circ \boldsymbol{\alpha_G}. \tag{3.11}$$

To handle the linear constraint and nonconvexity, we adopt the nonconvex alternating direction method of multipliers (ADMM) [58]. The iterative ADMM procedure decouples the original subproblem into two simpler updates, allowing efficient numerical solution while handling the linear constraint and nonconvexity of the problem. The augmented Lagrangian function (ALF) of problem (3.11) is

$$\mathcal{L}_\tau(\boldsymbol{u}, \boldsymbol{\alpha_G}; \boldsymbol{p}) = E(\boldsymbol{u}, \boldsymbol{\alpha_G}, \boldsymbol{v}^{n+1}) + \frac{\delta}{2}\|\boldsymbol{u} - \boldsymbol{u}^n\|_2^2 + \frac{\delta}{2}\|\boldsymbol{\alpha_G} - \boldsymbol{\alpha_G^n}\|_2^2 - \langle \boldsymbol{p}, \boldsymbol{u} - \boldsymbol{D_G} \circ \boldsymbol{\alpha_G} \rangle + \frac{\tau}{2}\|\boldsymbol{u} - \boldsymbol{D_G} \circ \boldsymbol{\alpha_G}\|_2^2,$$

where $\boldsymbol{p} \in \mathbb{R}^{N_1 \times N_2 \times 3}$ are the Lagrangian multipliers and $\tau > 0$ is a penalty parameter.

The ADMM algorithm consists of sequential updates of the variables as follows:

$$\begin{cases} \boldsymbol{\alpha_G^{\ell+1}} := \arg\min_{\alpha_G} \mathcal{L}_\tau(\boldsymbol{u}^\ell, \boldsymbol{\alpha_G}; \boldsymbol{p}^\ell), \\ \boldsymbol{u}^{\ell+1} := \arg\min_{\boldsymbol{u}} \mathcal{L}_\tau(\boldsymbol{u}, \boldsymbol{\alpha_G^{\ell+1}}; \boldsymbol{p}^\ell), \\ \boldsymbol{p}^{\ell+1} = \boldsymbol{p}^\ell - \tau(\boldsymbol{u}^{\ell+1} - (\boldsymbol{D_G} \circ \boldsymbol{\alpha_G})^{\ell+1}), \end{cases} \tag{3.12}$$

where ℓ denotes the inner ADMM iteration index.

Solving the $\boldsymbol{\alpha_G}$-subproblem in (3.12). The $\boldsymbol{\alpha_G}$-subproblem in (3.12) can be expressed as

$$\min_{\alpha_G} \frac{\tau}{2}\|\boldsymbol{D_G} \circ \boldsymbol{\alpha_G} - \boldsymbol{u}^\ell + \boldsymbol{p}^\ell/\tau\|_2^2 + \mu\|\boldsymbol{\alpha_G}\|_0 + \frac{\delta}{2}\|\boldsymbol{\alpha_G} - \boldsymbol{\alpha_G^n}\|_2^2.$$

By introducing the variables $\boldsymbol{x} = \boldsymbol{D_G} \circ \boldsymbol{\alpha_G}$ and $\boldsymbol{r} = \boldsymbol{u}^\ell - \boldsymbol{p}^\ell/\tau$, this problem can be equivalently reformulated as

$$\min_{\alpha_G} \frac{1}{2}\|\boldsymbol{x} - \boldsymbol{r}\|_2^2 + \frac{\mu}{\tau}\|\boldsymbol{\alpha_G}\|_0 + \frac{\delta}{2\tau}\|\boldsymbol{\alpha_G} - \boldsymbol{\alpha_G^n}\|_2^2. \tag{3.13}$$

The following proposition shows that, under suitable statistical assumptions, the total error $\|\boldsymbol{x} - \boldsymbol{r}\|_2^2$ can be well approximated by the sum of groupwise error terms: $\|\boldsymbol{x} - \boldsymbol{r}\|_2^2 \approx \sum_{k=1}^N \|\boldsymbol{x_{G_k}} - \boldsymbol{r_{G_k}}\|_2^2$, where $\boldsymbol{x_{G_k}}$ and $\boldsymbol{r_{G_k}}$ denote the components of $\boldsymbol{x}$ and $\boldsymbol{r}$ corresponding to the k-th group.

Proposition 3.2. *Let $\boldsymbol{x}$, $\boldsymbol{r} \in \mathbb{R}^{N_1\times N_2\times 3}$ and $\boldsymbol{x_{G_k}}$, $\boldsymbol{r_{G_k}} \in \mathbb{R}^{3P\times c}$ for $k = 1, 2, ..., N$. Assume that the elements of the error vector $\boldsymbol{e} = \boldsymbol{x} - \boldsymbol{r}$ are independent random variables with zero mean and variance σ^2. Then, for any $\varepsilon > 0$, the following holds:*

$$\lim_{\substack{B_1\to\infty\\ B_2\to\infty}} \boldsymbol{Pr}\left\{\left|\frac{1}{B_1}\|\boldsymbol{x} - \boldsymbol{r}\|_2^2 - \frac{1}{B_2}\sum_{k=1}^N \|\boldsymbol{x_{G_k}} - \boldsymbol{r_{G_k}}\|_2^2\right| < \varepsilon\right\} = 1,$$

where $\boldsymbol{Pr}(\cdot)$ denotes the probability, $B_1 = 3N_1N_2$, and $B_2 = 3P \cdot c \cdot N$.

Proof. The claim follows directly from the law of large numbers; see [39] for further details. □

Based on Proposition 1 and the identities

$$\|\boldsymbol{\alpha_G}\|_0 = \sum_{k=1}^N \|\boldsymbol{\alpha_{G_k}}\|_0 \quad \text{and} \quad \|\boldsymbol{\alpha_G}\|_2^2 = \sum_{k=1}^N \|\boldsymbol{\alpha_{G_k}}\|_2^2,$$

problem (3.13) can be equivalently expressed as

$$\min_{\alpha_G} \sum_{k=1}^N \left(\frac{1}{2}\|\boldsymbol{x_{G_k}} - \boldsymbol{r_{G_k}}\|_2^2 + \tilde{\tau}_1\|\boldsymbol{\alpha_{G_k}}\|_0 + \frac{\tilde{\tau}_2}{2}\|\boldsymbol{\alpha_{G_k}} - \boldsymbol{\alpha_{G_k}^n}\|_2^2\right),$$

where $\tilde{\tau}_1 = \frac{\mu B_2}{\tau B_1}$ and $\tilde{\tau}_2 = \frac{\delta B_2}{\tau B_1}$. This decomposition shows that the original problem (3.13) can be efficiently solved by minimizing N independent subproblems, each corresponding to a group $\boldsymbol{\alpha_{G_k}}$:

$$\min_{\alpha_{G_k}} \left\{\frac{1}{2}\|\boldsymbol{D_{G_k}}\boldsymbol{\alpha_{G_k}} - \boldsymbol{r_{G_k}}\|_2^2 + \tilde{\tau}_1\|\boldsymbol{\alpha_{G_k}}\|_0 + \frac{\tilde{\tau}_2}{2}\|\boldsymbol{\alpha_{G_k}} - \boldsymbol{\alpha_{G_k}^n}\|_2^2\right\}, \tag{3.14}$$

where $\boldsymbol{D_{G_k}}$ is the self-adaptive learned dictionary constructed from $\boldsymbol{r_{G_k}}$ as follows.

We first perform the SVD of $\boldsymbol{r_{G_k}}$:

$$\boldsymbol{r_{G_k}} = \boldsymbol{U_{G_k}}\boldsymbol{\Sigma_{G_k}}\boldsymbol{V_{G_k}^T} = \sum_{i=1}^m \gamma_{r_{G_k,i}}(\boldsymbol{u_{G_k,i}}\boldsymbol{v_{G_k,i}^T}), \tag{3.15}$$

where $\boldsymbol{\Sigma_{G_k}} = \text{diag}(\boldsymbol{\gamma_{r_{G_k}}})$ is a diagonal matrix with the singular values $\boldsymbol{\gamma_{r_{G_k}}} = [\gamma_{r_{G_k,1}}, \gamma_{r_{G_k,2}}, ..., \gamma_{r_{G_k,m}}]^T$ on its main diagonal and $m = \min(3P, c)$. The vectors $\boldsymbol{u_{G_k,i}}$ and $\boldsymbol{v_{G_k,i}}$ are the i-th columns of $\boldsymbol{U_{G_k}}$ and $\boldsymbol{V_{G_k}}$, respectively. The atoms of the dictionary are defined as $\boldsymbol{d_{G_k,i}} = \boldsymbol{u_{G_k,i}}\boldsymbol{v_{G_k,i}^T}$, and the learned dictionary $\boldsymbol{D_{G_k}}$ is formed as $\boldsymbol{D_{G_k}} = [\boldsymbol{d_{G_k,1}}, \boldsymbol{d_{G_k,2}}, \ldots, \boldsymbol{d_{G_k,m}}]$.

Since $\boldsymbol{r}_{\boldsymbol{G}_k} = \boldsymbol{D}_{\boldsymbol{G}_k}\boldsymbol{\gamma}_{\boldsymbol{r}_{\boldsymbol{G}_k}}$ from (3.15) and $\boldsymbol{D}_{\boldsymbol{G}_k}$ is unitary, the subproblem (3.14) reduces to

$$\min_{\boldsymbol{\alpha}_{\boldsymbol{G}_k}} \frac{1}{2}\|\boldsymbol{\alpha}_{\boldsymbol{G}_k} - \boldsymbol{\gamma}_{\boldsymbol{r}_{\boldsymbol{G}_k}}\|_2^2 + \tilde{\tau}_1\|\boldsymbol{\alpha}_{\boldsymbol{G}_k}\|_0 + \frac{\tilde{\tau}_2}{2}\|\boldsymbol{\alpha}_{\boldsymbol{G}_k} - \boldsymbol{\alpha}^n_{\boldsymbol{G}_k}\|_2^2,$$

which can be rewritten as

$$\min_{\boldsymbol{\alpha}_{\boldsymbol{G}_k}} \frac{1+\tilde{\tau}_2}{2}\left\|\boldsymbol{\alpha}_{\boldsymbol{G}_k} - \frac{\boldsymbol{\gamma}_{\boldsymbol{r}_{\boldsymbol{G}_k}} + \tilde{\tau}_2\boldsymbol{\alpha}^n_{\boldsymbol{G}_k}}{1+\tilde{\tau}_2}\right\|_2^2 + \tilde{\tau}_1\|\boldsymbol{\alpha}_{\boldsymbol{G}_k}\|_0.$$

This problem has the following closed-form hard-thresholding solution:

$$\boldsymbol{\alpha}_{\boldsymbol{G}_k} = \text{hard}\left(\mathbf{g}_{\mathbf{G}_k}, \rho\right) = \mathbf{g}_{\mathbf{G}_k} \odot \mathbf{1}\Big(|\mathbf{g}_{\mathbf{G}_k}| > \rho\Big), \tag{3.16}$$

where

$$\mathbf{g}_{\mathbf{G}_k} = (\boldsymbol{\gamma}_{\boldsymbol{r}_{\boldsymbol{G}_k}} + \tilde{\tau}_2\boldsymbol{\alpha}^n_{\boldsymbol{G}_k})/(1+\tilde{\tau}_2), \quad \rho = \sqrt{(2\tilde{\tau}_1)/(1+\tilde{\tau}_2)},$$

hard$(\cdot,\cdot)$ denotes the hard thresholding operator, $\odot$ is the elementwise multiplication, and $\mathbf{1}(\cdot)$ is the indicator function, which equals 1 when the condition is satisfied and 0 otherwise.

Consequently, the reconstructed group $\boldsymbol{x}_{\boldsymbol{G}_k}$ is obtained as $\boldsymbol{x}_{\boldsymbol{G}_k} = \boldsymbol{D}_{\boldsymbol{G}_k}\boldsymbol{\alpha}_{\boldsymbol{G}_k}$, using the coefficients from (3.16). Aggregating all reconstructed groups yields the image estimate $\boldsymbol{x} = \boldsymbol{D}_{\boldsymbol{G}} \circ \boldsymbol{\alpha}_{\boldsymbol{G}}$, as in (2.6).

Solving the $\boldsymbol{u}$-subproblem in (3.12). The $\boldsymbol{u}$-subproblem in (3.12) can be formulated as

$$\min_{\boldsymbol{u}} \left\{F(\boldsymbol{u}, \boldsymbol{v}^{n+1}) + \beta\,\text{SV-TV}(\boldsymbol{u}) + \frac{\delta}{2}\|\boldsymbol{u} - \boldsymbol{u}^n\|_2^2 + \frac{\tau}{2}\|\boldsymbol{u} - \mathbf{h}\|_2^2\right\},$$

where $\mathbf{h} = (\boldsymbol{D}_{\boldsymbol{G}} \circ \boldsymbol{\alpha}_{\boldsymbol{G}})^{\ell+1} + \boldsymbol{p}^\ell/\tau$. To facilitate the optimization, we introduce an auxiliary variable $\boldsymbol{w} = \boldsymbol{u}$ and equivalently rewrite

$$\min_{\boldsymbol{u},\boldsymbol{w}} \left\{F(\boldsymbol{u}, \boldsymbol{v}^{n+1}) + \beta\,\text{SV-TV}(\boldsymbol{w}) + \frac{\delta}{2}\|\boldsymbol{u} - \boldsymbol{u}^n\|_2^2 + \frac{\tau}{2}\|\boldsymbol{u} - \mathbf{h}\|_2^2\right\}, \quad \text{subject to:} \quad \boldsymbol{w} = \boldsymbol{u}. \tag{3.17}$$

The ALF corresponding to (3.17) is given by

$$\mathcal{L}_\xi(\boldsymbol{u}, \boldsymbol{w}; \boldsymbol{q}) = F(\boldsymbol{u}, \boldsymbol{v}^{n+1}) + \beta\,\text{SV-TV}(\boldsymbol{w}) + \frac{\delta}{2}\|\boldsymbol{u} - \boldsymbol{u}^n\|_2^2 + \frac{\tau}{2}\|\boldsymbol{u} - \mathbf{h}\|_2^2 - \langle \boldsymbol{q}, \boldsymbol{w} - \boldsymbol{u}\rangle + \frac{\xi}{2}\|\boldsymbol{w} - \boldsymbol{u}\|_2^2,$$

where $\boldsymbol{q} \in \mathbb{R}^{N_1 \times N_2 \times 3}$ is the Lagrangian multiplier and $\xi > 0$ is a penalty parameter. Applying the convex ADMM [59] to (3.17) results in the following iterative updates:

$$\begin{cases} \boldsymbol{u}^{t+1} := \arg\min_{\boldsymbol{u}} \left\{F(\boldsymbol{u}, \boldsymbol{v}^{n+1}) + \frac{\delta}{2}\|\boldsymbol{u} - \boldsymbol{u}^n\|_2^2 + \frac{\tau}{2}\|\boldsymbol{u} - \mathbf{h}\|_2^2 + \frac{\xi}{2}\|\boldsymbol{u} - \boldsymbol{w}^t + \boldsymbol{q}^t/\xi\|_2^2\right\}, \\ \boldsymbol{w}^{t+1} := \arg\min_{\boldsymbol{w}} \left\{\beta\,\text{SV-TV}(\boldsymbol{w}) + \frac{\xi}{2}\|\boldsymbol{w} - \boldsymbol{u}^{t+1} - \boldsymbol{q}^t/\xi\|_2^2\right\}, \\ \boldsymbol{q}^{t+1} = \boldsymbol{q}^t - \xi(\boldsymbol{w}^{t+1} - \boldsymbol{u}^{t+1}). \end{cases} \tag{3.18}$$

We first consider the $\boldsymbol{u}$-subproblem in (3.18). Since $F(\boldsymbol{u}, \boldsymbol{v}^{n+1})$ is strictly convex in $\boldsymbol{u}$ and the additional terms are quadratic, the objective function admits a unique minimizer. However, due to the complexity of the data-fidelity term, a closed-form solution is not available. This subproblem can be efficiently solved using Newton's method, with the following update formula:

$$\boldsymbol{u}^{j+1} = \boldsymbol{u}^{j} - \frac{1 - (\boldsymbol{f} - \boldsymbol{v}^{n+1})\exp(-\boldsymbol{u}^{j}) + \delta(\boldsymbol{u}^{j} - \boldsymbol{u}^{n}) + \tau(\boldsymbol{u}^{j} - \mathbf{h}) + \xi(\boldsymbol{u}^{j} - \boldsymbol{w}^{t} + \boldsymbol{q}^{t}/\xi)}{(\boldsymbol{f} - \boldsymbol{v}^{n+1})\exp(-\boldsymbol{u}^{j}) + \delta + \tau + \xi}, \tag{3.19}$$

where j denotes the iteration index of Newton's method.

Next, we consider the $\boldsymbol{w}$-subproblem in (3.18). Using the orthogonal matrix

$$\mathbf{P} = \begin{bmatrix} \frac{1}{\sqrt{2}}\mathbf{I} & -\frac{1}{\sqrt{2}}\mathbf{I} & \mathbf{0} \\ \frac{1}{\sqrt{6}}\mathbf{I} & \frac{1}{\sqrt{6}}\mathbf{I} & -\frac{2}{\sqrt{6}}\mathbf{I} \\ \frac{1}{\sqrt{3}}\mathbf{I} & \frac{1}{\sqrt{3}}\mathbf{I} & \frac{1}{\sqrt{3}}\mathbf{I} \end{bmatrix},$$

where $\mathbf{I} \in \mathbb{R}^{N_1 \times N_2}$ is the identity matrix, we define $z = \mathbf{P}\boldsymbol{w}$ and $\mathbf{s} = \mathbf{P}(\boldsymbol{u}^{t+1} + \boldsymbol{q}^{t}/\xi)$. Under this transformation, the $\boldsymbol{w}$-subproblem in (3.18) can be equivalently rewritten as

$$\min_{z} \frac{\xi}{2}\|z - \mathbf{s}\|_2^2 + \beta\,(\|\nabla\hat{z}\|_1 + \alpha\|\nabla z_3\|_1), \tag{3.20}$$

where $\hat{z} = (z_1, z_2)$ and $\nabla\hat{z} = (\nabla z_1, \nabla z_2)$. To handle the nondifferentiable terms, we introduce auxiliary variables $\boldsymbol{d}_1$ and $\boldsymbol{d}_2$, thereby transforming problem (3.20) into the following constrained form:

$$\min_{z,\boldsymbol{d}_1,\boldsymbol{d}_2} \frac{\xi}{2}\|z - \mathbf{s}\|_2^2 + \beta\,(\|\boldsymbol{d}_1\|_1 + \alpha\|\boldsymbol{d}_2\|_1), \quad \text{subject to:} \quad \boldsymbol{d}_1 = \nabla\hat{z}, \quad \boldsymbol{d}_2 = \nabla z_3. \tag{3.21}$$

The ALF corresponding to problem (3.21) is given by

$$\begin{aligned} \mathcal{L}_\theta(z, \boldsymbol{d}_1, \boldsymbol{d}_2; \boldsymbol{b}_1, \boldsymbol{b}_2) \;=\; & \frac{\xi}{2}\|z - \mathbf{s}\|_2^2 + \beta\,(\|\boldsymbol{d}_1\|_1 + \alpha\|\boldsymbol{d}_2\|_1) - \langle \boldsymbol{b}_1, \boldsymbol{d}_1 - \nabla\hat{z}\rangle + \frac{\theta}{2}\|\boldsymbol{d}_1 - \nabla\hat{z}\|_2^2 \\ & -\langle \boldsymbol{b}_2, \boldsymbol{d}_2 - \nabla z_3\rangle + \frac{\theta}{2}\|\boldsymbol{d}_2 - \nabla z_3\|_2^2, \end{aligned}$$

where $\boldsymbol{b}_1 \in (\mathbb{R}^{N_1 \times N_2 \times 3 \times})^2$ and $\boldsymbol{b}_2 \in \mathbb{R}^{N_1 \times N_2 \times 3}$ are the Lagrangian multipliers and $\theta > 0$ is a penalty parameter. Applying the ADMM to problem (3.21) yields the following iterative updates:

$$\begin{cases} z^{j+1} := \arg\min_z \mathcal{L}_\theta(z, \boldsymbol{d}_1^j, \boldsymbol{d}_2^j; \boldsymbol{b}_1^j, \boldsymbol{b}_2^j), \\ (\boldsymbol{d}_1^{j+1}, \boldsymbol{d}_2^{j+1}) := \arg\min_{\boldsymbol{d}_1,\boldsymbol{d}_2} \mathcal{L}_\theta(z^{j+1}, \boldsymbol{d}_1, \boldsymbol{d}_2; \boldsymbol{b}_1^j, \boldsymbol{b}_2^j), \\ \boldsymbol{b}_1^{j+1} = \boldsymbol{b}_1^j - \theta(\boldsymbol{d}_1^{j+1} - \nabla\hat{z}^{j+1}), \\ \boldsymbol{b}_2^{j+1} = \boldsymbol{b}_2^j - \theta(\boldsymbol{d}_2^{j+1} - \nabla z_3^{j+1}). \end{cases} \tag{3.22}$$

The z-subproblem in (3.22) can be equivalently expressed as

$$\min_{z} \frac{\xi}{2}\|z - s\|_2^2 + \frac{\theta}{2}\|\nabla\hat{z} - \boldsymbol{d}_1^j + \boldsymbol{b}_1^j/\theta\|_2^2 + \frac{\theta}{2}\|\nabla z_3 - \boldsymbol{d}_2^j + \boldsymbol{b}_2^j/\theta\|_2^2.$$

Applying the first-order optimality condition, z satisfies the following normal equations:

$$\begin{aligned} (\xi + \theta\nabla^T\nabla)z_i &= \xi s_i + \theta\nabla^T(\boldsymbol{d}_{1,i}^j - \boldsymbol{b}_{1,i}^j/\theta), \quad i = 1, 2, \\ (\xi + \theta\nabla^T\nabla)z_3 &= \xi s_3 + \theta\nabla^T(\boldsymbol{d}_2^j - \boldsymbol{b}_2^j/\theta), \end{aligned} \tag{3.23}$$

where $\nabla^T = -\mathrm{div}$ and the discrete divergence operator is defined by

$$\mathrm{div}(s_1, s_2) = \partial_{x_1} s_1 + \partial_{x_2} s_2.$$

Assuming periodic boundary conditions, the linear system in (3.23) can be efficiently solved in closed form using the two-dimensional discrete Fourier transform (DFT).

The $(\boldsymbol{d}_1, \boldsymbol{d}_2)$-subproblem in (3.22) can be decomposed into two independent subproblems, one for each variable. Specifically, the subproblems for $\boldsymbol{d}_1$ and $\boldsymbol{d}_2$ are given by

$$\begin{aligned} \boldsymbol{d}_1^{j+1} &:= \arg\min_{\boldsymbol{d}_1} \beta\|\boldsymbol{d}_1\|_1 + \frac{\theta}{2}\|\boldsymbol{d}_1 - (\nabla \hat{z}^{j+1} + \boldsymbol{b}_1^j/\theta)\|_2^2, \\ \boldsymbol{d}_2^{j+1} &:= \arg\min_{\boldsymbol{d}_2} \alpha\beta\|\boldsymbol{d}_2\|_1 + \frac{\theta}{2}\|\boldsymbol{d}_2 - (\nabla z_3{}^{j+1} + \boldsymbol{b}_2^j/\theta)\|_2^2. \end{aligned}$$

These are standard ℓ_1-regularized quadratic problems, whose solutions are given by the soft-thresholding (shrinkage) operator. Thus, we have

$$\boldsymbol{d}_1^{j+1} = shrink\Big(\nabla \hat{z}^{j+1} + \frac{\boldsymbol{b}_1^j}{\theta}, \frac{\beta}{\theta}\Big), \quad \boldsymbol{d}_2^{j+1} = shrink\Big(\nabla z_3^{j+1} + \frac{\boldsymbol{b}_2^j}{\theta}, \frac{\alpha\beta}{\theta}\Big), \tag{3.24}$$

where $shrink(\cdot)$ is defined elementwise as

$$shrink(\mathbf{a}, b)_s = \frac{\mathbf{a}_s}{\|\mathbf{a}_s\|_2} \cdot \max(\|\mathbf{a}_s\|_2 - b, 0), \quad s \in \Omega.$$

The overall algorithm for solving the proposed model (3.3) is summarized in Algorithm 1.

Algorithm 1 Solving the proposed model (3.3).

```
Input: choose the parameters $\lambda, \mu, \alpha, \beta, \delta, \tau, \xi, \theta > 0$, patch size $P$, similar patch number $c$, window size $L$, stride $S$, maximum iteration numbers $\tilde{N}_{out}$, $\tilde{N}_{\boldsymbol{u},out}$, $\tilde{N}_{\boldsymbol{u},in}$, $\tilde{N}_{\boldsymbol{u},Newton}$, $\tilde{N}_z$, tolerance values $tol_{out}$, $tol_{\boldsymbol{u},out}$, $tol_{\boldsymbol{u},in}$, $tol_{\boldsymbol{u},Newton}$, $tol_z$.
Initialization: set $\boldsymbol{u}^0 = \log(\max(\boldsymbol{f}, \epsilon))$ with $\epsilon > 0$, $\boldsymbol{\alpha}_{\boldsymbol{G}}^0 = \boldsymbol{0}$, $\boldsymbol{v}^0 = \boldsymbol{0}$, $\boldsymbol{p}^0 = \boldsymbol{q}^0 = \boldsymbol{0}$, $\boldsymbol{b}_i^0 = \boldsymbol{0}$ $(i = 1, 2)$.
repeat
    Compute $\boldsymbol{v}^{n+1}$ as in (3.10).
    Compute $\boldsymbol{u}^{n+1}$ by iterating $\ell = 1, 2, ..., \tilde{N}_{\boldsymbol{u},out}$:
        Compute $\boldsymbol{x}^{\ell+1} = (\boldsymbol{D_G} \circ \boldsymbol{\alpha_G})^{\ell+1}$ with $\boldsymbol{D}_{\boldsymbol{G}_k}$ and $\boldsymbol{\alpha}_{\boldsymbol{G}_k}$ obtained from (3.15) and (3.16).
        Compute $\boldsymbol{u}^{\ell+1}$ by iterating $t = 1, 2, ..., \tilde{N}_{\boldsymbol{u},in}$:
            Compute $\boldsymbol{u}^{t+1}$ using Newton's method as in (3.19),
            Let $\mathbf{s} = \mathbf{P}(\boldsymbol{u}^{t+1} + \boldsymbol{q}^t/\xi)$,
            Compute $z^{t+1}$ by iterating $j = 1, 2, ..., \tilde{N}_z$:
                compute $z^{j+1}$ by solving (3.23) using DFT,
                compute $\boldsymbol{d}_1^{j+1}$ and $\boldsymbol{d}_2^{j+1}$ as in (3.24),
                compute $\boldsymbol{b}_1$ and $\boldsymbol{b}_2$ as in (3.22),
            Let $\boldsymbol{w}^{t+1} = \mathbf{P}^T z^{t+1}$.
            Update $\boldsymbol{q}^{t+1} = \boldsymbol{q}^t - \xi(\boldsymbol{w}^{t+1} - \boldsymbol{u}^{t+1})$,
        Update $\boldsymbol{p}^{\ell+1} = \boldsymbol{p}^\ell - \tau(\boldsymbol{u}^{\ell+1} - \boldsymbol{x}^{\ell+1})$.
until a stopping criterion is satisfied.
Output: restored image $e^{\boldsymbol{u}}$.
```

4. Experimental results

This section presents the experimental results of the proposed model and compares its performance with several existing approaches, including L2-SVTV [26], AA-SVTV [13], and SO-L2-SVTV [23]. These methods incorporate SVTV with the L^2 data-fidelity term, the term in (2.2), and the term in (2.3), respectively. For a fair comparison, L2-SVTV and AA-SVTV were implemented using a variable splitting strategy and solved via the ADMM framework. All numerical experiments were performed in MATLAB R2025a on a 64-bit Windows 11 workstation equipped with a 3.6 GHz Intel CPU and 64 GB of RAM.

4.1. Implementation settings

We evaluate each model on 11 natural images and 7 SAR images, as shown in Figure 2. The intensity range of all original images is assumed to be [0, 255]. In our experiments, we consider six mixed noise configurations (M, σ), where the multiplicative Gamma noise takes values $M = 20$, 10, 5, and the additive Gaussian noise levels are $\sigma = 20$ and 30. Because the Gaussian component can introduce nonpositive pixel values in the observed data $\boldsymbol{f}$ and the AA-SVTV model requires strictly positive inputs, we define $\tilde{\boldsymbol{f}} = \max(\boldsymbol{f}, 10^{-5})$ and use $\tilde{\boldsymbol{f}}$ only for AA-SVTV. For all other models, including the proposed one, we use the original observed data $\boldsymbol{f}$ without modification. All numerical results are provided in the supplementary material available at `https://buly.kr/8Ix7tH0`. Source code is available at `https://github.com/mjungHUFS/SO-L2-SVTV-GSR`.

(a) Airplane (b) Baboon (c) Barbara (d) Boat (e) Butterfly (f) Castle

(g) Cathedral (h) Hill (i) Lena (j) Policemen (k) Statues (l) SAR1

(m) SAR2 (n) SAR3 (o) SAR4 (p) SAR5 (q) SAR6 (r) SAR7

Figure 2. Original test images. (a)–(d), (i): 256×256, (e): 321×481, (f), (g), (j), (k): 481×321, (h): 201×266, (k): 278×350, (l)–(r): 512×512.

To assess the performance of the models, we compute the peak signal-to-noise ratio (PSNR):

$$\mathrm{PSNR}(\boldsymbol{u}, \boldsymbol{u}_*) = 10 \log_{10}\left(\frac{3N_1N_2 \times 255^2}{\|\boldsymbol{u} - \boldsymbol{u}_*\|_2^2}\right),$$

where $\boldsymbol{u}$ and $\boldsymbol{u}_*$ denote the restored and original images, respectively, and N_1N_2 is the total number of pixels. We also evaluate the structural similarity (SSIM) index [60], a perceptually motivated metric that accounts for structural information in the visual scene. For color images, we report the SSIM value obtained by averaging the SSIM scores computed over the three RGB channels. For each model, all parameters are tuned to achieve the best restoration results with respect to both visual fidelity and the quantitative PSNR and SSIM metrics.

All models are terminated once the following stopping condition is satisfied:

$$\frac{\|\mathbf{g}^{\text{iter}} - \mathbf{g}^{\text{iter}-1}\|_2}{\|\mathbf{g}^{\text{iter}}\|_2} < \text{tol} \qquad \text{or} \qquad n > \tilde{N},$$

where $\mathbf{g} \in \{\boldsymbol{u}, \boldsymbol{z}\}$, $\text{tol} > 0$ denotes the prescribed tolerance and $\tilde{N} > 0$ is the maximum number of iterations. For the proposed model, we set $\text{tol} = 5 \times 10^{-3}$ and $\tilde{N} = 15$ for the outer loop. To mitigate the additional computational cost introduced by the GSR module, the number of outer iterations for $\boldsymbol{u}$ is restricted to $\tilde{N}_{\boldsymbol{u},out} = 1$, which is sufficient to maintain reconstruction quality. For the inner loops associated with $\boldsymbol{u}$, we set $\tilde{N}_{\boldsymbol{u},in} = \tilde{N}_{\boldsymbol{u},newton} = 5$, while the inner loop for $\boldsymbol{z}$ is limited to $\tilde{N}_z = 10$. All inner loops use a tolerance of 10^{-3}. For the SO-L2-SVTV model, we adopt the stopping criteria reported in [23], using $\text{tol} = 10^{-3}$ and a maximum of $\tilde{N} = 100$ outer iterations; details of the inner loop settings can be found in the cited reference. For the L2-SVTV and AA-SVTV models, we set $\text{tol} = 10^{-4}$ and $\tilde{N} = 200$ for the outer loop. The inner loop of the AA-SVTV model employs the same tolerance and iteration limits as those used in [23]. For the SO-L2-SVTV and the proposed models, we initialize $\boldsymbol{u}$ as $\boldsymbol{u}^0 = \log(\max(\boldsymbol{f}, 1))$, whereas for the L2-SVTV and AA-SVTV models, we set $\boldsymbol{u}^0 = \boldsymbol{f}$ and $\tilde{\boldsymbol{f}}$, respectively.

The parameter settings for the proposed model are summarized as follows. For the GSR representation, the image patch size is set to 6 × 6 for natural images except Statues and to 5 × 5 for SAR images and Statues. The number of similar patches c is fixed at 80, resulting in a group matrix of size 108 × 80 or 75 × 80. The search window is set to 20 × 20 pixels, and the overlap between adjacent patches is $S = 4$ pixels. The GSR regularization parameters μ and τ control sparsity strength. In general, larger values of μ or τ produce smoother reconstructions, although increasing τ also increases the computational cost. To balance reconstruction quality and efficiency, we fix $\tau = 1$. The SVTV parameter α is set to 0.6 for all experiments. The parameter λ, which penalizes the Gaussian noise component, also affects smoothness: smaller values of λ yield smoother restored images. In our experiments, we use $\lambda = 0.001$ by default, except for $(M, \sigma) = (20, 30)$ and $(10, 30)$, where $\lambda = 0.0005$, and $(M, \sigma) = (5, 20)$, where $\lambda = 0.002$. The regularization parameters μ and β have a primary impact on restoration quality. The parameter β, governing the SVTV strength, is selected from $\{0.1, 0.2, 0.3\}$ based on noise level and image characteristics. For instance, we use $\beta \in \{0.1, 0.2\}$ for $(M, \sigma) = (20, 20)$ and $(20, 30)$; $\beta = 0.2$ for $(M, \sigma) = (10, 20)$; $\beta \in \{0.2, 0.3\}$ for $(M, \sigma) = (10, 30)$; $\beta = 0.3$ for $(M, \sigma) = (5, 20)$ and $(5, 30)$. The optimal value of μ is influenced by the noise level, the characteristics of the underlying image, and the selected value of β. In general, μ is chosen from the range $\{0.01, 0.02, \ldots, 0.12\}$. The specific (μ, β) values used in each experiment are provided in the corresponding figure. Finally, we set the proximal parameter δ to a small value, 10^{-6}, since a small δ allows the iterates to move more freely along descent directions, reducing the damping effect of the proximal term and often leading to faster practical convergence. The ADMM parameters ξ and θ, used for updating $\boldsymbol{u}$ and $\boldsymbol{z}$, respectively, are fixed at 1.

4.2. *Denoising results on natural color images*

Figure 3 presents the denoising results of all models for noise levels $M = 20, 10, 5$ with $\sigma = 20$. AA-SVTV reduces the mixed noise to some extent but introduces artifacts, such as white or black dots in the sky regions. It also tends to oversmooth dark areas, such as the lower part of the boat, particularly at higher noise levels, which degrades the overall tone quality of the restored images. L2-SVTV suppresses both noise types more effectively than AA-SVTV; however, it does not completely remove noise in bright regions, such as the sky, and may produce erroneous color values as M increases. Dark regions are also oversmoothed, similar to AA-SVTV. These effects are more evident in the zoomed-in images shown in Figure 4. In contrast, SO-L2-SVTV effectively reduces noise in both dark and bright regions while preserving structural details, such as the lines and lower parts of the boat. The restored images exhibit improved visual quality compared to AA-SVTV and L2-SVTV, with better overall tone preservation, highlighting the benefits of the data-fidelity term used in SO-L2-SVTV, which is also incorporated in the proposed model. Nevertheless, SO-L2-SVTV exhibits staircasing artifacts in smooth regions, particularly in the sky, a known limitation of TV-based regularization. The proposed model, which incorporates GSR regularization, alleviates these artifacts while preserving more image details and producing cleaner results than SO-L2-SVTV. This improvement also yields the highest PSNR and SSIM values among all models. These results demonstrate the effectiveness of combining the data-fidelity term with SVTV and GSR regularization for removing both multiplicative and Gaussian noise.

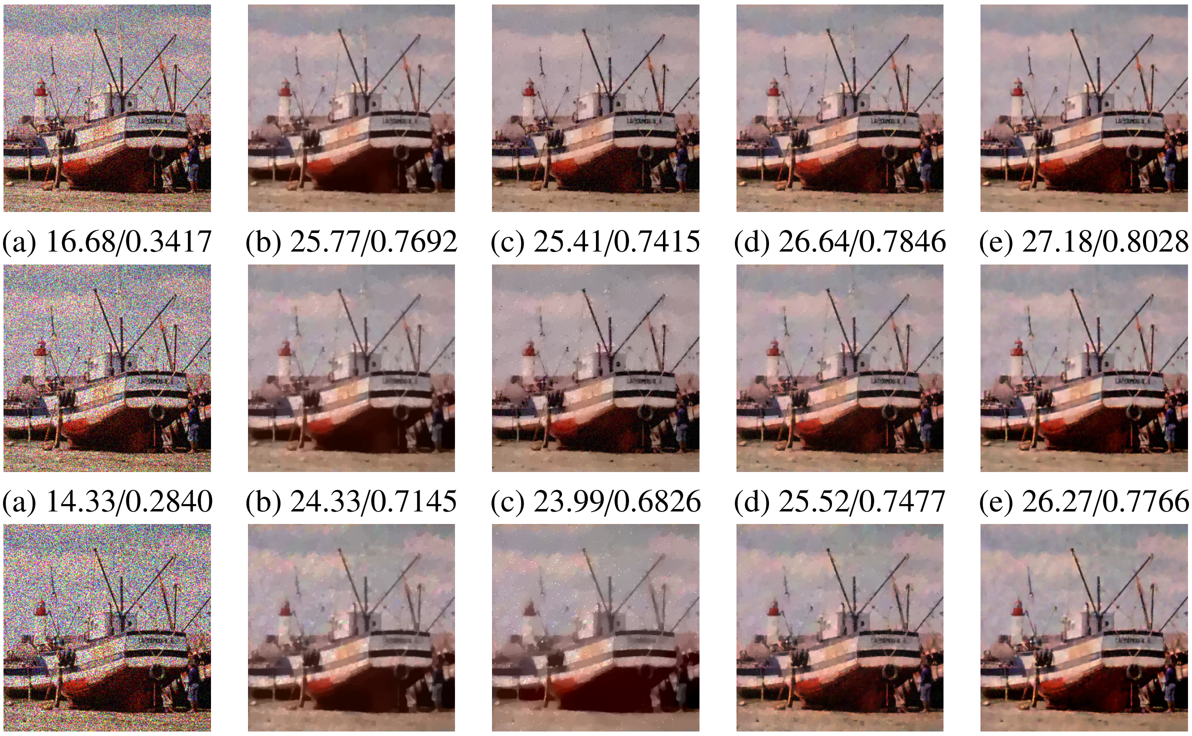

(a) 16.68/0.3417 (b) 25.77/0.7692 (c) 25.41/0.7415 (d) 26.64/0.7846 (e) 27.18/0.8028

(a) 14.33/0.2840 (b) 24.33/0.7145 (c) 23.99/0.6826 (d) 25.52/0.7477 (e) 26.27/0.7766

(a) 11.73/0.2258 (b) 23.24/0.6582 (c) 22.03/0.5742 (d) 24.42/0.7088 (e) 25.09/0.7411

Figure 3. Denoising results at noise levels $M = 20, 10, 5$ (from top to bottom) and $\sigma = 20$. (a) Data f; (b) L2-SVTV; (c) AA-SVTV; (d) SO-L2-SVTV; (e) Proposed. Parameters (μ, β) for (e) (from top to bottom): $(0.02, 0.2)$, $(0.04, 0.2)$, $(0.06, 0.3)$.

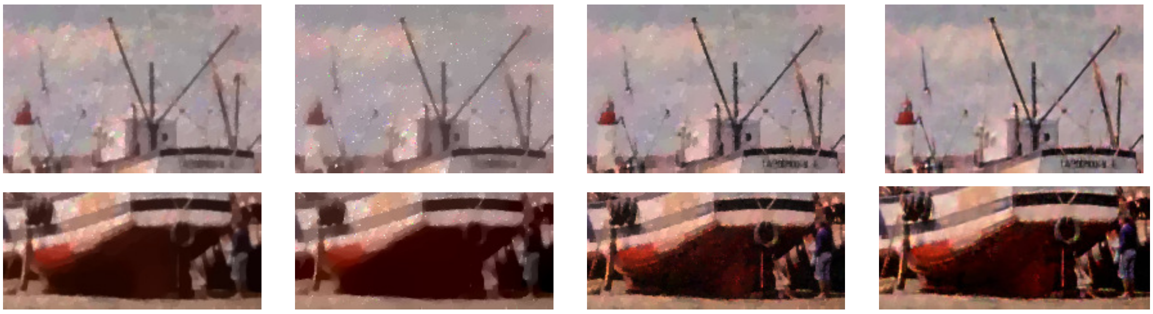
L2-SVTV AA-SVTV SO-L2-SVTV Proppposed

Figure 4. Zoomed-in regions from Figure 3 for the noise level $(M, \sigma) = (5, 20)$.

Figures 5 and 6 present the denoising results at high noise levels, specifically $(M, \sigma) = (10, 30)$, $(5, 20)$, and $(5, 30)$. Similar to the previous results, AA-SVTV exhibits artifacts, such as white dots and color distortions in bright regions, which are visible in the wing area of Butterfly, the headscarf in Barbara, and the sky and tower regions in Policemen. These issues are clearly visible in the zoomed-in patches shown in Figure 7. L2-SVTV eliminates the white-dot artifacts but still fails to adequately denoise bright regions, resulting in misleading color values. Both AA-SVTV and L2-SVTV also oversmooth dark regions, including the textured background in Barbara and the tree and grass areas in Policemen. In contrast, SO-L2-SVTV achieves more effective denoising across the entire image, preserving details and textures while avoiding color artifacts, demonstrating the advantage of the SO-L2 data-fidelity term. Nevertheless, it produces noticeable staircasing artifacts in smooth regions, such as the background of Butterfly, the face area of Barbara, and the sky of Policemen, caused by the SVTV regularization. The proposed model substantially reduces these artifacts while further preserving textures, such as the headscarf in Barbara and the tree and tower regions in Policemen, resulting in more natural-looking restored images. It also achieves significantly higher PSNR and SSIM values compared to the other models. These results highlight the effectiveness of incorporating GSR and collectively validate the superiority of the proposed model for removing mixed multiplicative and Gaussian noise.


(a) 14.48/0.3332 (b) 22.92/0.7998 (c) 21.52/0.7624 (d) 23.41/0.8030 (e) 24.52/0.8518

(a) 12.44/0.1863 (b) 23.96/0.6172 (c) 22.93/0.5444 (d) 24.48/0.6625 (e) 25.51/0.7154

Figure 5. Denoising results at noise levels $(M, \sigma) = (10, 30)$ (top) and $(5, 20)$ (bottom). (a) Data f; (b) L2-SVTV; (c) AA-SVTV; (d) SO-L2-SVTV; (e) Proposed. Parameters (μ, β) for (e): top-$(0.07, 0.2)$; bottom-$(0.07, 0.3)$.

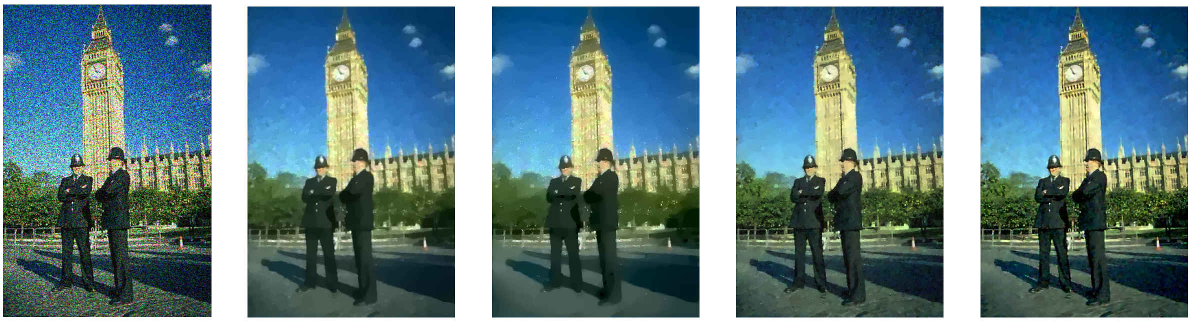

(a) 12.50/0.2276 (b) 21.70/0.6548 (c) 20.99/0.5973 (d) 22.49/0.6998 (e) 23.69/0.7447

Figure 6. Denoising results at noise level $(M,\sigma) = (5,30)$. (a) Data $\boldsymbol{f}$; (b) L2-SVTV; (c) AA-SVTV; (d) SO-L2-SVTV; (e) Proposed. Parameters (μ,β) for (e): $(0.08, 0.3)$.

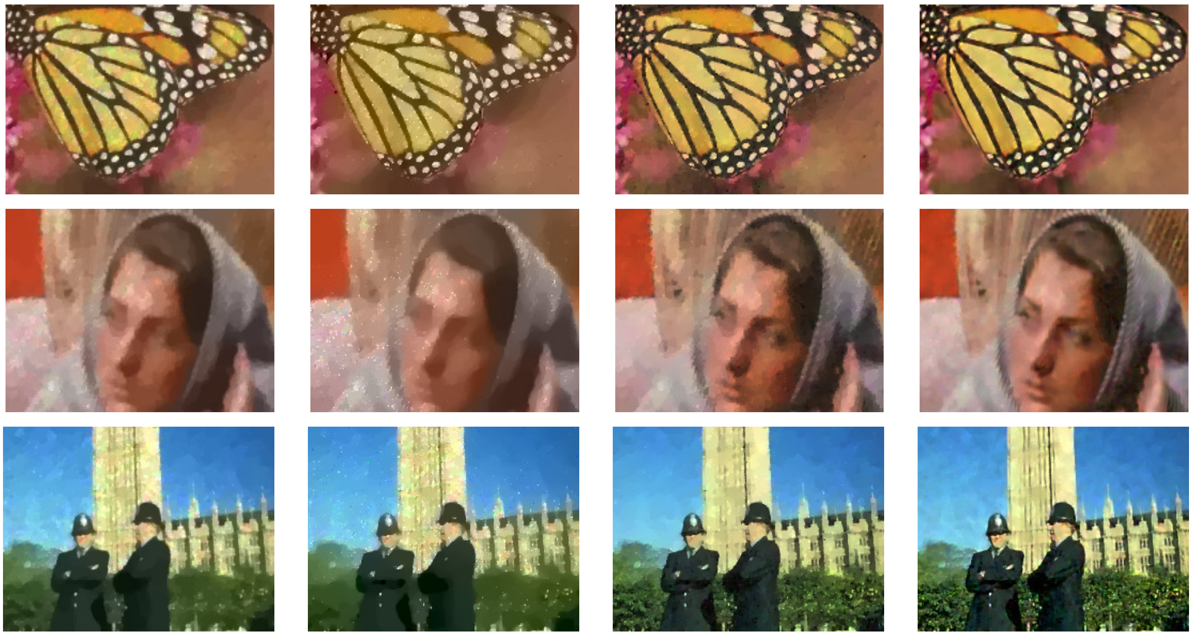

L2-SVTV AA-SVTV SO-L2-SVTV Proposed

Figure 7. Zoom-in regions from Figures 5 and 6.

In Figure 8, we illustrate the effect of the $\boldsymbol{v}$ term in the proposed model by comparing the reconstruction results obtained with and without this term at noise levels $(M,\sigma) = (20,30)$ and $(10,30)$. When $\boldsymbol{v} = 0$, the data-fidelity term requires $\boldsymbol{f} > 0$; thus, we use the cropped data $\tilde{\boldsymbol{f}} = \max(\boldsymbol{f}, 10^{-5})$ in place of $\boldsymbol{f}$. Even with this adjustment, the model without the $\boldsymbol{v}$ term fails to adequately remove the mixed noise in dark regions. This deficiency is clearly visible in the upper sky, clothing, and shadow regions in Policemen, the body areas in Statues, the lower part of the ship in Boat, and the right-hand tree regions in Hill, as shown in the zoomed-in images in Figure 9. Although increasing μ and β can reduce noise in these areas, doing so leads to excessive smoothing elsewhere, thereby degrading the overall reconstruction quality. By contrast, the full proposed model, which includes the $\boldsymbol{v}$ term, effectively suppresses mixed noise across both dark and bright regions. Even with relatively small values of μ and β, the model adequately eliminates noise in dark areas, better preserving fine details and textures and achieving significantly higher PSNR and SSIM values. This improvement is evident in the tower region in Policemen, the pebble areas in Statues, and the roof regions in Hill. These enhancements arise because the $\boldsymbol{v}$ term explicitly extracts the Gaussian noise component, facilitating more accurate removal of both noise types. Overall, the results highlight the importance of the $\boldsymbol{v}$ term and validate the effectiveness of the proposed data-fidelity formulation in properly separating multiplicative Gamma noise from additive Gaussian noise.

(a) 23.43/0.6587 (b) 25.32/0.8035 (a) 22.83/0.5968 (b) 24.73/0.7031

(a) 24.59/0.7043 (b) 25.69/0.7561 (a) 24.69/0.5824 (b) 26.01/0.6640

Figure 8. Effect of the $\boldsymbol{v}$ term in the data-fidelity term (3.2) of the proposed model. Top: $(M,\sigma) = (20,30)$; bottom: $(10,30)$. (a) Without the $\boldsymbol{v}$ term (i.e., $\boldsymbol{v} = 0$); (b) With the $\boldsymbol{v}$ term. Parameters (μ,β) for (a): top-$(0.1,0.3)$, $(0.04,0.3)$; bottom-$(0.08,0.3)$, $(0.14,0.3)$. Parameters (μ,β) for (b): top-$(0.05,0.2)$, $(0.03,0.2)$; bottom-$(0.06,0.2)$, $(0.03,0.3)$.

Figure 9. Zoomed-in regions from Figure 8. Top: without the $\boldsymbol{v}$ term; bottom: with the $\boldsymbol{v}$ term.

Figure 10 illustrates the effect of the SVTV term in the proposed model and its complementary interaction with GSR at noise level $(M, \sigma) = (10, 20)$. Specifically, we compare the proposed model with and without the SVTV term, as well as the SO-L2-SVTV model. When the SVTV term is removed, the proposed model reduces to a GSR-only regularization. This variant effectively preserves textures and fine details but performs poorly in homogeneous regions, where unreliable patch grouping leads to residual noise or oversmoothing. Typical artifacts include residual noise in the eye regions and the left-hand black fur of Baboon, as well as oversmoothing in the face of Barbara and the lips of Lena. In contrast, the SO-L2-SVTV model, which relies solely on local SVTV regularization, effectively denoises homogeneous regions and preserves major edges. However, it tends to oversmooth textured areas and introduces noticeable staircasing artifacts in smooth regions. By jointly incorporating GSR and SVTV, the proposed model benefits from nonlocal texture preservation and local piecewise-smooth regularization while mitigating their respective limitations. As a result, it achieves improved visual quality across both textured and homogeneous regions, along with higher PSNR and SSIM values. These results demonstrate the complementary roles of GSR and SVTV in the proposed model.


(a) 25.94/0.7596 (b) 25.46/0.7164 (c) 26.69/0.7673

(a) 21.92/0.6389 (b) 21.99/0.5867 (c) 22.67/0.6499

(a) 26.27/0.7888 (b) 25.99/0.7621 (c) 27.43/0.8066

Figure 10. Effect of the SVTV term in the proposed model at noise level $(M, \sigma) = (10, 20)$. (a) Proposed model without the SVTV term; (b) SO-L2-SVTV; (c) Proposed model. Parameters (μ, β) for (c) (from top to bottom): $(0.05, 0.2)$, $(0.03, 0.2)$, $(0.06, 0.2)$.

In Figure 11, we illustrate the effects of the parameters λ, μ, and β at a noise level $(M, \sigma) = (10, 30)$.

The top row shows denoising results for $\beta = 0.1$ and $\mu \in \{0.06, 0.07, 0.08, 0.09, 0.10\}$, while the middle row shows results for $\beta = 0.2$ and $\mu \in \{0.03, 0.04, 0.05, 0.06, 0.07\}$, with λ fixed at 0.0005 in both cases. The bottom row illustrates the effect of varying $\lambda \in \{0.0001, 0.0002, 0.0005, 0.001, 0.002\}$, with (μ, β) fixed at $(0.05, 0.2)$. From the first two rows, it can be observed that increasing μ reduces noise but also smooths fine details. Based on PSNR and SSIM values, the optimal μ is 0.08 for $\beta = 0.1$ and 0.05 for $\beta = 0.2$. Increasing β leads to stronger smoothing, which slightly decreases PSNR values but enhances noise suppression near edges, resulting in clearer edges and higher SSIM values. Considering both visual quality and quantitative metrics, $(\mu, \beta) = (0.05, 0.2)$ is selected as the overall optimal setting. From the bottom row, increasing λ preserves more image details, yielding higher PSNR values, but also introduces additional noise, lowering SSIM values. The restored images for $\lambda \in \{0.0005, 0.001, 0.002\}$ appear visually similar, with correspondingly similar PSNR and SSIM values. Taking both quantitative metrics into account, we select $\lambda = 0.0005$ as the optimal value. In practice, the choice of λ is less critical than that of μ and β; for example, $\lambda = 0.001$ generally provides satisfactory denoising, though minor adjustments may be needed depending on the noise level. By contrast, μ and β primarily govern the overall smoothness of the restored image and are more sensitive, requiring careful tuning according to the noise characteristics and image content.

24.77/0.7401 $(0.06, 0.1)$
24.99/0.7463 $(0.07, 0.1)$
25.05/0.7475 $(0.08, 0.1)$
25.05/0.7473 $(0.09, 0.1)$
25.00/0.7454 $(0.1, 0.1)$

24.71/0.7426 $(0.03, 0.2)$
24.92/0.7506 $(0.04, 0.2)$
24.93/0.7508 $(\mathbf{0.05}, \mathbf{0.2})$
24.89/0.7503 $(0.06, 0.2)$
24.83/0.7488 $(0.07, 0.2)$

24.31/0.7604 $(\lambda = 0.0001)$
24.76/0.7560 $(\lambda = 0.0002)$
24.93/0.7508 $(\lambda = \mathbf{0.0005})$
24.95/0.7486 $(\lambda = 0.001)$
24.90/0.7463 $(\lambda = 0.002)$

Figure 11. Effect of the parameters λ, μ, and β at noise level $(M, \sigma) = (10, 30)$. Top and middle rows: $\lambda = 0.0005$ with varying (μ, β); bottom row: $(\mu, \beta) = (0.05, 0.2)$ with varying λ. The best denoising result is obtained using $(\mu, \beta) = (0.05, 0.2)$ and $\lambda = 0.0005$.

4.3. *Denoising results on real SAR images*

Figure 12 presents the denoising results on real SAR images at $(M, \sigma) = (5, 20)$. These SAR images contain numerous dark regions, such as trees and shadows, as well as bright regions, including buildings, cars, and ships. Similar to the results observed for natural color images, AA-SVTV introduces white artifacts in bright regions and tends to oversmooth dark regions. L2-SVTV reduces the mixed noise more effectively; however, it still oversmooths dark areas and fails to fully denoise bright regions, resulting in inaccurate color values. In contrast, SO-L2-SVTV successfully suppresses mixed noise in both dark and bright regions while better preserving structural details, leading to higher PSNR and SSIM values compared to AA-SVTV and L2-SVTV. The proposed model further enhances the denoising performance by mitigating staircasing artifacts, effectively removing mixed noise, and preserving fine details. As a result, it produces cleaner images than SO-L2-SVTV and achieves the highest PSNR and SSIM values. These results demonstrate the superior denoising capability of the proposed model, even when applied to real SAR images.

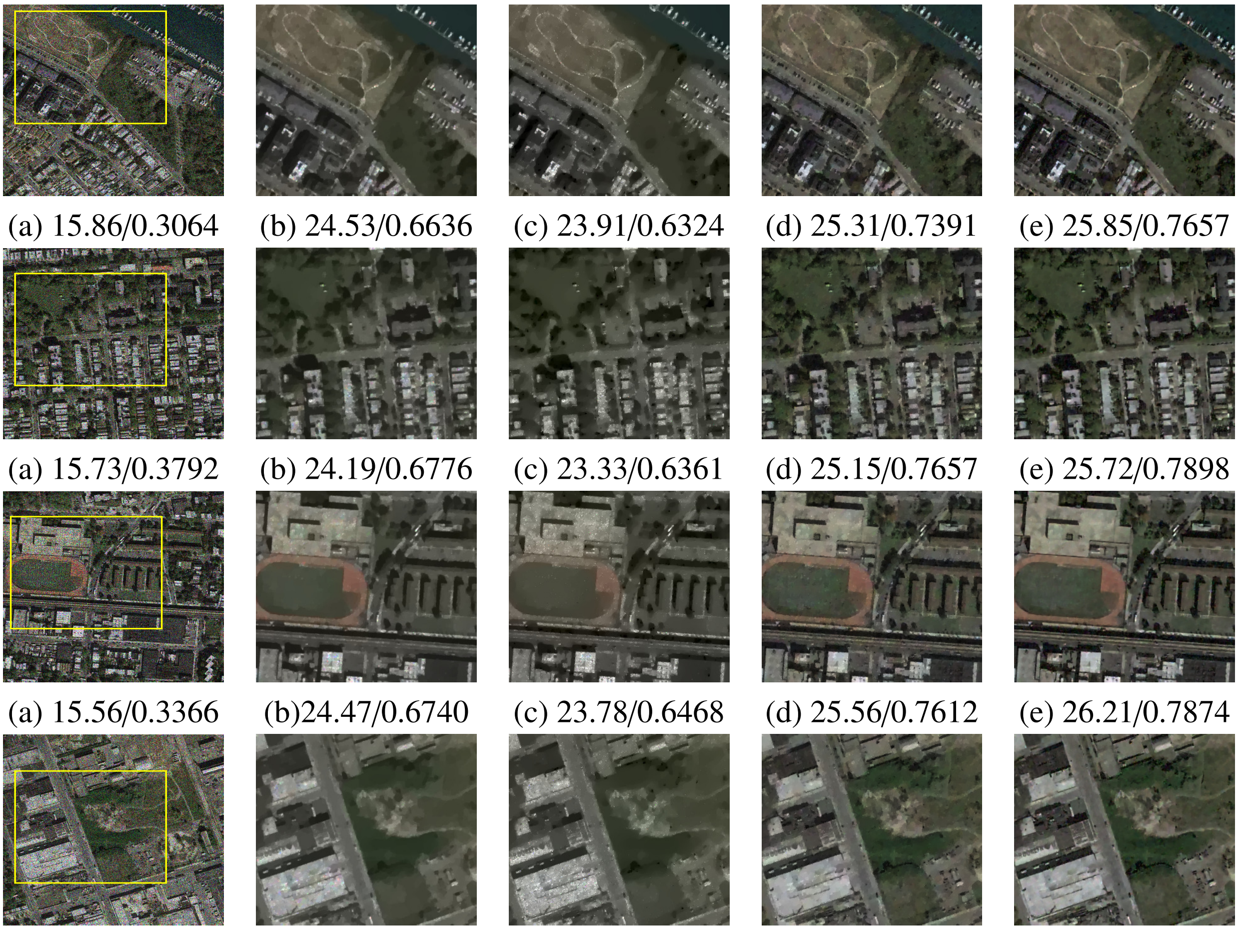

(a) 15.86/0.3064 (b) 24.53/0.6636 (c) 23.91/0.6324 (d) 25.31/0.7391 (e) 25.85/0.7657

(a) 15.73/0.3792 (b) 24.19/0.6776 (c) 23.33/0.6361 (d) 25.15/0.7657 (e) 25.72/0.7898

(a) 15.56/0.3366 (b)24.47/0.6740 (c) 23.78/0.6468 (d) 25.56/0.7612 (e) 26.21/0.7874

(a) 14.64/0.2431 (b) 24.91/0.6458 (c) 24.36/0.6270 (d) 25.76/0.7117 (e) 26.29/0.7397

Figure 12. Zoomed-in regions of the restored images at noise level $(M, \sigma) = (5, 20)$. (a) Data f with zoomed-in regions; (b) L2-SVTV; (c) AA-SVTV; (d) SO-L2-SVTV; (e) Proposed. Parameters (μ, β) for (e) (from top to bottom): $(0.07, 0.3)$, $(0.09, 0.3)$, $(0.08, 0.3)$, $(0.07, 0.3)$.

In Figure 13, we compare the proposed model with a BM3D-based method at $(M, \sigma) = (5, 30)$. Since SAR-BM3D [7] cannot be directly applied to images with additive Gaussian noise, we first use color BM3D (CBM3D) [61] to suppress the Gaussian noise and then apply SAR-BM3D to each RGB channel to remove multiplicative Gamma noise. We refer to this as CBM3D+SAR-BM3D. CBM3D+SAR-BM3D effectively reduces the mixed noise while preserving edges and structural details; however, it introduces color artifacts near edges, as shown in the zoomed-in regions in Figure 14. This results in lower PSNR and SSIM values compared to the proposed model. In contrast, the proposed model produces well-denoised images with preserved details and without the color artifacts observed in CBM3D+SAR-BM3D. Moreover, CBM3D+SAR-BM3D requires precise knowledge of the noise levels σ and M, whereas the proposed model achieves effective denoising without this information by setting $\gamma = 1$. Overall, these results highlight the superior denoising performance and robustness of the proposed model compared to the BM3D-based approach.

(a) 24.24/0.6862 (b) 24.88/0.7073 (a) 22.88/0.6912 (b) 23.88/0.7372

(a) 26.40/0.7475 (b) 26.95/0.7622 (a) 24.69/0.6493 (b) 25.91/0.7080

Figure 13. Comparison of the proposed model with CBM3D+SAR-BM3D at noise level $(M, \sigma) = (5, 30)$. (a) CBM3D+SAR-BM3D; (b) Proposed with $\gamma = 1$. Parameters (μ, β) for (b): top-$(0.12, 0.3)$, $(0.1, 0.3)$; bottom-$(0.11, 0.3)$, $(0.08, 0.3)$.

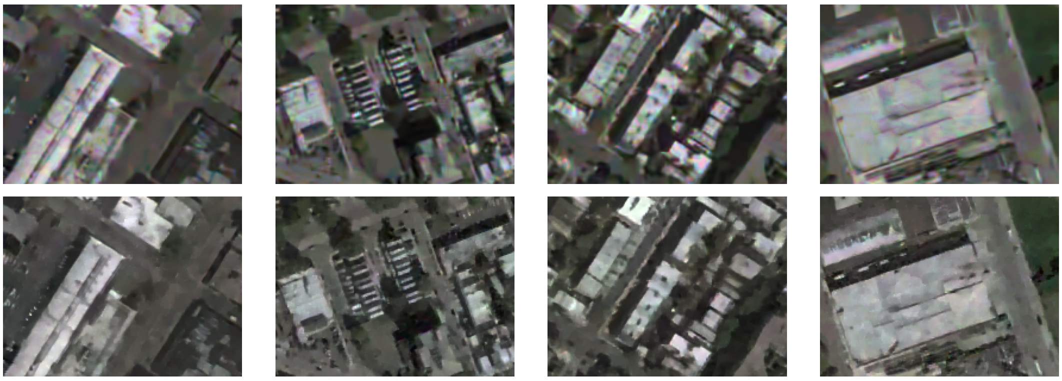

Figure 14. Zoomed-in regions from Figure 13. Top: CBM3D+SAR-BM3D; bottom: Proposed.

Figure 15 illustrates the evolution of the PSNR values, together with the relative errors of $\boldsymbol{u}$ and $\boldsymbol{v}$ generated by the proposed model, as functions of the outer iteration index n, under noise levels $(M, \sigma) = (10, 20)$ and $(5, 20)$. As the iteration proceeds, the relative errors of both $\boldsymbol{u}$ and $\boldsymbol{v}$ decrease monotonically, indicating stable and consistent updates of the estimated variables. Meanwhile, the PSNR values increase rapidly in the early iterations and gradually converge to steady plateaus, reflecting the progressive improvement and stabilization of the reconstructed images. This convergence behavior demonstrates the numerical stability of the proposed algorithm and the consistent enhancement of reconstruction quality across iterations. Moreover, the observed monotonic error decay and PSNR stabilization provide empirical evidence supporting the theoretical convergence guarantees established in the analysis.

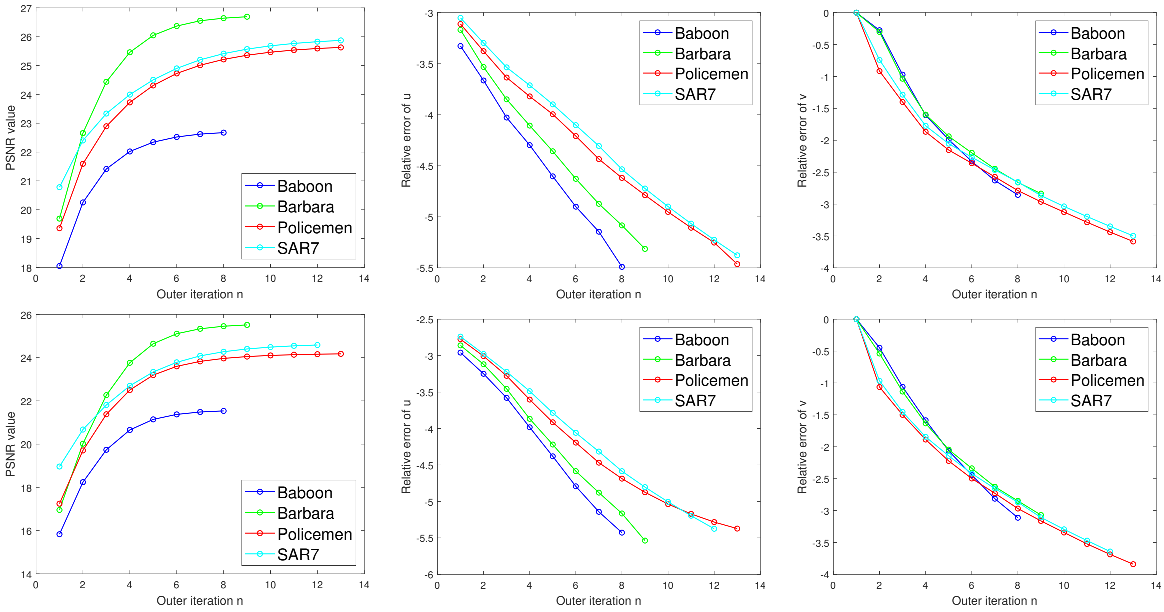

(a) (b) (c)

Figure 15. Plots of PSNR and relative errors versus the outer iteration n at noise levels $(M, \sigma) = (10, 20)$ (top) and $(5, 20)$ (bottom). (a) PSNR values of the restored images $\exp(\boldsymbol{u}^n)$; (b) $\log\left(\|\boldsymbol{u}^n - \boldsymbol{u}^{n-1}\|_2 / \|\boldsymbol{u}^n\|_2\right)$; (c) $\log\left(\|\boldsymbol{v}^n - \boldsymbol{v}^{n-1}\|_2 / \|\boldsymbol{v}^n\|_2\right)$.

In Tables 1 and 2, we report the PSNR and SSIM values of all models at noise levels $M = 20, 10, 5$ and $\sigma = 20, 30$. The proposed model produces similar PSNR and SSIM values whether $\gamma = (M-1)/M$ or $\gamma = 1$ in the data-fidelity term, indicating that high-quality results can be achieved without prior knowledge of the multiplicative noise level. The parameter γ regulates the relative contribution of the multiplicative noise component. Larger γ values enforce the multiplicative likelihood more strongly, yielding smoother reconstructions and higher PSNR but slightly lower SSIM due to suppression of fine textures and weak edges; smaller γ values preserve more structural detail while retaining some residual noise. In all experiments, we adopt $\gamma = (M-1)/M$ according to the assumed number of looks in the Gamma noise model, although comparable results can be obtained with $\gamma = 1$. Despite these variations, the proposed method consistently achieves the highest PSNR and SSIM values across all noise levels, confirming its robustness and superiority over existing approaches.

Table 1. PSNR and SSIM values for all models at noise levels $M = 20, 10, 5$ and $\sigma = 20$.

Image	Data f	L2-SVTV	AA-SVTV	SO-L2-SVTV	Proposed ($\gamma = \frac{M-1}{M}$)	Proposed ($\gamma = 1$)
$M = 20, \sigma = 20$						
Airplane	14.78/0.2323	25.18/0.7670	24.78/0.7360	25.68/0.8065	26.85/0.7942	**26.90/0.7943**
Baboon	16.81/0.4765	22.37/0.5986	22.28/0.6411	22.89/0.6465	23.94/**0.7127**	**23.97**/0.7106
Barbara	17.27/0.3215	25.92/0.7272	25.09/0.6860	26.46/0.7578	28.05/0.8111	**28.06/0.8127**
Boat	16.68/0.3417	25.77/0.7692	25.41/0.7415	26.64/0.7846	27.18/**0.8028**	**27.20**/0.7986
Butterfly	17.67/0.4365	24.66/0.8526	23.28/0.7831	25.43/0.8533	26.58/**0.8940**	**26.61**/0.8938
Castle	17.10/0.2453	27.29/0.7921	26.01/0.7527	27.85/0.8170	**28.47**/0.8409	28.46/**0.8425**
Cathedral	16.85/0.3125	25.35/0.7557	24.95/0.7451	25.93/0.7923	**26.56/0.7833**	26.53/0.7825
Hill	17.96/0.3464	26.46/0.6709	25.15/0.6290	27.20/0.7286	27.52/0.7280	**27.58/0.7292**
Lena	16.66/0.2803	26.55/0.7670	25.61/0.7623	26.92/0.7840	28.64/0.8322	**28.74/0.8358**
Policemen	17.76/0.3812	24.81/0.7848	24.03/0.7334	25.28/0.8015	26.62/0.8397	**26.63/0.8442**
Statues	18.15/0.4718	24.55/0.6498	24.78/0.7159	25.40/0.7516	25.86/0.7775	**25.94/0.7788**
SAR1	19.56/0.4575	26.63/0.7538	26.73/0.7721	27.35/0.8116	27.87/0.8222	**27.90/0.8246**
SAR2	19.28/0.5802	25.33/0.7779	25.33/0.7960	26.20/0.8394	26.72/**0.8516**	**26.74**/0.8502
SAR3	19.55/0.4435	26.51/0.7532	26.66/0.7714	27.19/0.8028	27.84/0.8186	**27.86/0.8198**
SAR4	20.07/0.3557	28.46/0.7885	28.05/0.7815	29.07/0.8274	29.72/0.8405	**29.80/0.8437**
SAR5	19.48/0.5255	26.38/0.7771	26.11/0.7863	27.10/0.8288	27.68/**0.8451**	**27.72**/0.8444
SAR6	19.36/0.4766	26.82/0.7767	26.52/0.7831	27.53/0.8241	28.23/0.8400	**28.31/0.8405**
SAR7	18.78/0.3875	27.13/0.7506	27.05/0.7578	27.89/0.7938	28.34/0.8074	**28.42/0.8083**
Average	17.99/0.3929	25.90/0.7506	25.43/0.7430	26.56/0.7917	27.37/0.8134	**27.41/0.8140**
$M = 10, \sigma = 20$						
Airplane	12.19/0.1786	23.96/0.7178	22.99/0.6035	24.56/0.7583	25.36/**0.7484**	**25.43**/0.7477
Baboon	14.48/0.3836	21.45/0.5212	21.16/0.5527	21.99/0.5867	22.67/**0.6499**	**22.75**/0.6432
Barbara	15.03/0.2545	25.00/0.6732	24.05/0.6210	25.46/0.7164	26.69/0.7673	**26.78/0.7700**
Boat	14.33/0.2840	24.33/0.7145	23.99/0.6826	25.52/0.7477	26.27/**0.7766**	**26.35**/0.7690
Butterfly	15.53/0.3781	23.21/0.8136	22.12/0.7389	24.19/0.8288	25.17/**0.8722**	**25.22**/0.8709
Castle	14.81/0.1936	25.81/0.7595	24.73/0.6957	26.70/0.7992	27.59/0.8201	**27.69/0.8239**
Cathedral	14.55/0.2492	23.88/0.7051	23.62/0.6813	24.56/0.7485	25.59/**0.7585**	**25.61**/0.7572
Hill	15.83/0.2819	25.20/0.6045	24.11/0.5585	26.40/0.6971	26.77/0.7003	**26.91/0.7047**
Lena	14.36/0.2248	25.46/0.7277	24.54/0.7003	25.99/0.7621	27.43/**0.8066**	**27.50**/0.8053
Policemen	15.63/0.3298	23.00/0.7176	22.73/0.6760	24.22/0.7754	25.63/0.8230	**25.73/0.8291**
Statues	16.11/0.3997	23.30/0.5692	23.48/0.6486	24.53/0.7112	24.97/**0.7449**	**25.15**/0.7443
SAR1	17.97/0.4012	25.55/0.7081	25.52/0.7248	26.60/0.7932	27.06/0.8064	**27.15/0.8075**
SAR2	17.56/0.5143	24.22/0.7276	24.09/0.7406	25.31/0.8145	25.87/**0.8338**	**25.99**/0.8311
SAR3	17.94/0.3825	25.75/0.7247	25.52/0.7225	26.44/0.7806	27.03/**0.8017**	**27.10**/0.8013
SAR4	18.69/0.3095	27.53/0.7593	27.03/0.7462	28.42/0.8123	28.90/0.8273	**29.03/0.8294**
SAR5	17.85/0.4620	25.31/0.7307	24.97/0.7338	26.19/0.8018	26.85/**0.8248**	**26.90**/0.8188
SAR6	17.70/0.4143	25.64/0.7271	25.36/0.7320	26.66/0.7982	27.41/**0.8199**	**27.48**/0.8164
SAR7	16.93/0.3187	26.03/0.6993	25.86/0.7056	26.92/0.7591	27.45/**0.7785**	**27.55**/0.7763
Average	15.97/0.3311	24.70/0.7000	24.22/0.6814	25.59/0.7606	26.37/**0.7867**	**26.46**/0.7859
$M = 5, \sigma = 20$						
Airplane	9.44/0.1292	22.72/0.6373	20.93/0.4727	23.19/0.7187	23.60/**0.6686**	**23.69**/0.6683
Baboon	11.87/0.2870	20.51/0.4307	19.86/0.3828	21.15/0.5334	21.54/**0.5594**	**21.61**/0.5502
Barbara	12.44/0.1863	23.96/0.6172	22.93/0.5444	24.48/0.6625	25.51/**0.7154**	**25.58**/0.7147
Boat	11.73/0.2258	23.24/0.6582	22.03/0.5742	24.42/0.7088	25.09/**0.7411**	**25.16**/0.7262
Butterfly	13.01/0.3061	21.45/0.7582	20.67/0.7209	22.76/0.7923	23.55/**0.8333**	**23.61**/0.8310
Castle	12.25/0.1405	24.51/0.7193	23.01/0.6301	25.42/0.7589	26.14/**0.7789**	**26.18**/0.7759
Cathedral	11.92/0.1831	22.67/0.6577	22.01/0.5928	23.41/0.7008	24.17/**0.7084**	**24.24**/0.7083
Hill	13.40/0.2136	24.31/0.5578	22.97/0.4829	25.45/0.6539	25.87/0.6631	**25.99/0.6660**
Lena	11.69/0.1686	24.04/0.6861	22.82/0.6063	24.75/0.7251	25.99/**0.7579**	**26.07**/0.7555
Policemen	13.14/0.2699	22.00/0.6664	21.28/0.6102	22.94/0.7346	24.17/**0.7778**	**24.21**/0.7777
Statues	13.71/0.3143	22.24/0.4973	21.81/0.5489	23.54/0.6657	23.66/**0.6869**	**23.91**/0.6867
SAR1	15.89/0.3277	24.39/0.6576	23.88/0.6440	25.28/0.7483	25.84/**0.7714**	**25.86**/0.7650
SAR2	15.41/0.4256	23.02/0.6664	22.16/0.6116	24.00/0.7666	24.58/**0.7958**	**24.70**/0.7883
SAR3	15.86/0.3064	24.53/0.6636	23.91/0.6324	25.31/0.7391	25.85/**0.7657**	**25.92**/0.7610
SAR4	16.78/0.2516	26.46/0.7220	25.63/0.6890	27.33/0.7827	27.90/**0.8002**	**27.95**/0.7997
SAR5	15.73/0.3792	24.19/0.6776	23.33/0.6361	25.15/0.7657	25.72/**0.7898**	**25.73**/0.7771
SAR6	15.56/0.3366	24.47/0.6740	23.78/0.6468	25.56/0.7612	26.21/**0.7874**	**26.31**/0.7813
SAR7	14.64/0.2431	24.91/0.6458	24.36/0.6270	25.76/0.7117	26.29/**0.7397**	**26.40**/0.7366
Average	13.58/0.2608	23.53/0.6441	22.63/0.5918	24.44/0.7183	25.09/**0.7412**	**25.17**/0.7372

* The bolded values denote the best denoising performance.

Table 2. PSNR and SSIM values for all models at noise levels $M = 20, 10, 5$ and $\sigma = 30$.

Image	Data f	L2-SVTV	AA-SVTV	SO-L2-SVTV	Proposed ($\gamma = \frac{M-1}{M}$)	Proposed ($\gamma = 1$)
$M = 20, \sigma = 30$						
Airplane	13.88/0.2034	24.76/0.7609	23.59/0.6518	25.23/0.7865	26.13/0.7963	**26.20/0.7964**
Baboon	15.45/0.4003	22.12/0.5847	21.26/0.5330	22.37/0.6225	23.00/**0.6600**	**23.07**/0.6556
Barbara	15.79/0.2542	25.28/0.6975	25.49/0.7043	24.33/0.6573	26.80/**0.7602**	**26.73**/0.7586
Boat	15.37/0.2870	25.04/0.7431	23.90/0.6895	25.63/0.7420	**26.13/0.7641**	26.08/0.7577
Butterfly	16.06/0.3756	23.83/0.8290	22.09/0.7885	24.30/0.8053	**25.32/0.8675**	25.19/0.8664
Castle	15.68/0.1921	26.55/0.7917	25.60/0.7481	26.63/0.7859	**27.11/0.8123**	27.02/0.8110
Cathedral	15.48/0.2589	24.70/0.7341	24.26/0.6992	24.82/0.7559	**25.56/0.7539**	25.50/0.7521
Hill	16.24/0.2590	25.64/0.6325	24.75/0.5905	26.15/0.6701	26.44/0.6713	**26.47/0.6747**
Lena	15.33/0.2281	26.11/0.7495	24.42/0.7025	26.12/0.7584	**27.61/0.8062**	27.55/0.8053
Policemen	16.12/0.3086	23.65/0.7474	23.34/0.7067	23.83/0.7394	**25.32/0.8035**	25.24/0.8024
Statues	16.39/0.3651	23.81/0.6046	24.03/0.6685	24.32/0.6843	24.73/**0.7031**	**24.75**/0.7000
SAR1	17.27/0.3461	25.22/0.6879	25.39/0.7140	25.67/0.7416	26.35/**0.7530**	**26.45**/0.7614
SAR2	17.10/0.4663	24.12/0.7196	24.22/0.7398	24.80/0.7809	25.45/0.8044	**25.50/0.8045**
SAR3	17.26/0.3386	25.25/0.6949	25.48/0.7174	25.66/0.7344	**26.48**/0.7598	26.46/**0.7646**
SAR4	17.56/0.2516	27.27/0.7445	26.76/0.7291	27.61/0.7736	28.20/0.7903	**28.21/0.7949**
SAR5	17.22/0.4088	25.21/0.7237	24.99/0.7387	25.51/0.7641	26.36/**0.7956**	**26.37**/0.7946
SAR6	17.16/0.3677	25.26/0.7069	25.39/0.7362	25.96/0.7626	**26.93/0.7940**	**26.93**/0.7937
SAR7	16.79/0.2978	25.90/0.6902	26.15/0.7138	26.53/0.7349	27.16/0.7558	**27.18/0.7566**
Average	16.23/0.3116	24.98/0.7135	24.51/0.6984	25.30/0.7389	**26.17/0.7695**	26.16/**0.7695**
$M = 10, \sigma = 30$						
Airplane	11.66/0.1619	23.67/0.7185	22.58/0.5773	24.15/0.7629	24.93/**0.7508**	**25.06/0.7508**
Baboon	13.65/0.3345	21.29/0.5082	20.46/0.4369	21.59/0.5499	22.24/**0.6064**	**22.29**/0.5925
Barbara	14.06/0.2083	24.75/0.6601	23.80/0.6081	24.91/0.6789	**25.55/0.7100**	25.47/0.7058
Boat	13.51/0.2439	24.01/0.7032	23.00/0.6415	24.99/0.7205	25.69/**0.7561**	**25.70**/0.7441
Butterfly	14.48/0.3332	22.92/0.7998	21.52/0.7624	23.41/0.8030	**24.52/0.8518**	24.44/0.8485
Castle	13.94/0.1582	25.54/0.7546	24.51/0.7018	26.00/0.7684	**26.58**/0.7984	26.56/**0.7985**
Cathedral	13.66/0.2141	23.59/0.6936	23.12/0.6513	24.09/0.7275	**24.71/0.7346**	24.69/0.7322
Hill	14.73/0.2200	25.10/0.6006	23.95/0.5330	25.73/0.6548	26.01/**0.6640**	**26.07**/0.6633
Lena	13.47/0.1888	24.99/0.7200	23.73/0.6653	25.38/0.7456	26.73/0.7860	**26.80/0.7865**
Policemen	14.57/0.2739	22.74/0.7070	22.30/0.6608	23.14/0.7258	**24.68**/0.7837	24.65/**0.7857**
Statues	14.92/0.3164	23.05/0.5546	23.06/0.6093	23.76/0.6560	24.01/0.6818	**24.27/0.6828**
SAR1	16.25/0.3099	24.88/0.6754	24.68/0.6834	25.25/0.7282	25.62/0.7389	**25.82/0.7457**
SAR2	15.99/0.4212	23.72/0.7039	23.30/0.6987	24.27/0.7640	24.77/**0.7891**	**24.93**/0.7848
SAR3	16.24/0.3001	24.71/0.6663	24.72/0.6775	25.25/0.7188	25.83/0.7428	**25.83/0.7435**
SAR4	16.72/0.2262	26.69/0.7243	26.14/0.7076	27.08/0.7635	27.54/0.7803	**27.65/0.7839**
SAR5	16.19/0.3678	24.42/0.6820	24.19/0.6942	25.08/0.7472	25.70/**0.7791**	**25.82**/0.7738
SAR6	16.09/0.3289	24.64/0.6764	24.63/0.6963	25.36/0.7393	26.28/**0.7793**	**26.41**/0.7764
SAR7	15.54/0.2561	25.32/0.6641	25.35/0.6763	26.08/0.7191	26.56/0.7383	**26.57/0.7346**
Average	14.76/0.2702	24.22/0.6785	23.61/0.6490	24.75/0.7207	25.44/**0.7484**	**25.50**/0.7463
$M = 5, \sigma = 30$						
Airplane	9.13/0.1199	22.57/0.6652	20.81/0.4568	23.12/0.7106	23.58/**0.6807**	**23.74**/0.6795
Baboon	11.38/0.2569	20.34/0.4152	19.70/0.3611	20.90/0.5215	21.23/**0.5324**	**21.31**/0.5124
Barbara	11.92/0.1575	23.91/0.6158	22.88/0.5491	24.24/0.6489	25.06/0.6854	**25.13/0.6903**
Boat	11.24/0.1964	22.62/0.6449	21.81/0.5694	24.00/0.6830	24.61/**0.7207**	**24.74**/0.7048
Butterfly	12.40/0.2774	21.15/0.7421	20.43/0.7070	22.47/0.7634	**23.30/0.8173**	23.24/0.8128
Castle	11.73/0.1202	24.26/0.7219	22.95/0.6346	25.01/0.7484	25.72/0.7565	**25.76/0.7650**
Cathedral	11.43/0.1631	22.61/0.6501	21.94/0.5847	23.12/0.6865	23.89/**0.6942**	**23.98**/0.6928
Hill	12.71/0.1734	24.15/0.5495	22.92/0.4744	25.07/0.6253	25.26/0.6224	**25.41/0.6303**
Lena	11.23/0.1464	24.05/0.6792	22.76/0.6093	24.54/0.7166	**25.72/0.7499**	**25.72**/0.7447
Policemen	12.50/0.2276	21.70/0.6548	20.99/0.5973	22.49/0.6998	**23.69**/0.7447	23.66/**0.7484**
Statues	12.99/0.2567	22.45/0.5325	21.73/0.5198	23.11/0.6242	23.23/**0.6362**	**23.42**/0.6294
SAR1	14.75/0.2609	24.18/0.6440	23.57/0.6220	24.68/0.7070	**25.02/0.7154**	24.88/0.7073
SAR2	14.40/0.3583	22.78/0.6525	21.85/0.5926	23.14/0.7087	**23.94/0.7553**	23.88/0.7372
SAR3	14.73/0.2504	24.28/0.6528	23.47/0.6060	24.54/0.6921	**25.10/0.7190**	25.03/0.7140
SAR4	15.41/0.1912	26.00/0.6999	25.20/0.6657	26.60/0.7484	26.94/0.7557	**26.95/0.7622**
SAR5	14.64/0.3118	23.71/0.6484	22.92/0.6091	24.37/0.7203	**24.98/0.7506**	24.82/0.7293
SAR6	14.51/0.2746	24.17/0.6565	23.39/0.6179	24.75/0.7149	**25.47/0.7488**	25.41/0.7375
SAR7	13.78/0.2038	24.67/0.6310	24.18/0.6078	25.27/0.6803	25.77/**0.7097**	**25.91**/0.7080
Average	12.83/0.2193	23.31/0.6365	22.42/0.5769	23.97/0.6889	24.58/**0.7108**	**24.61**/0.7059

* The bolded values denote the best denoising performance.

4.4. Algorithm complexity and computational cost

The computational complexity of the proposed model is dominated by the GSR operations performed on overlapping patches of size P, together with pixel-wise data-fidelity and SVTV computations. Let $\hat{N} = N_1 N_2$ denote the total number of image pixels and S the patch stride. The total number of patches is approximately $N \approx \hat{N}/S^2$. For each patch, the average cost of searching for similar patches is denoted by T_s. The SVD of the grouped patch matrix of size $3P \times c$ has a computational cost of $O(3P \cdot c \cdot m)$ per patch, where $m = \min(3P, c)$. Sparse coding and reconstruction reduce to multiplying the unitary dictionary $\boldsymbol{D}_{\boldsymbol{G}_k} \in \mathbb{R}^{3P \times c \times m}$ by the coefficient vector $\boldsymbol{\alpha}_{\boldsymbol{G}_k} \in \mathbb{R}^m$, which also requires $O(3P \cdot c \cdot m)$ operations per patch. Including pixel-wise operations such as data-fidelity and SVTV computation, the overall complexity per iteration can be expressed as

$$O\left(\frac{\hat{N}}{S^2}(T_s + 3P \cdot c \cdot m) + \hat{N}\right).$$

Since S is a small fixed constant, the complexity simplifies to

$$O\left(\hat{N}(T_s + 3P \cdot c \cdot m)\right),$$

indicating that the GSR operations dominate the total computation.

The computational costs of all methods are reported in Table 3, particularly for the noise level $(M, \sigma) = (10, 20)$. For the proposed model, the total number of outer iterations is also indicated. Although the proposed model achieves the best denoising performance, it has the highest computational cost, mainly due to the nonlocal patch search, the SVDs of grouped patches, and the subsequent sparse coding and reconstruction of each group. These operations dominate the computational complexity but can be efficiently parallelized, offering the potential for substantial runtime reduction. Future work could focus on improving efficiency through approximate or reduced-complexity nonlocal patch search and more efficient implementations of both SVD and sparse coding.

Table 3. Computational time (in seconds) for all models at noise level $(M, \sigma) = (10, 20)$.

Image	Image size	L2-SVTV	AA-SVTV	SO-L2-SVTV	Proposed ($\tilde{N}_{out}$)
Airplane	256 × 256	1.54	5.26	0.42	44.53 (6)
Baboon	256 × 256	1.77	5.31	0.52	59.23 (8)
Barbara	256 × 256	1.54	5.33	0.51	77.53 (9)
Boat	256 × 256	1.78	5.32	0.89	106.71 (12)
Butterfly	321 × 481	1.47	4.60	0.47	59.99 (10)
Castle	481 × 321	5.46	14.84	1.28	161.24 (9)
Cathedral	481 × 321	5.35	14.76	1.25	166.58 (8)
Hill	201 × 266	2.47	7.57	1.00	116.15 (11)
Lena	256 × 256	1.58	5.37	0.53	66.51 (9)
Policemen	481 × 321	5.40	15.17	2.16	250.77 (13)
Statues	278 × 350	5.42	14.56	2.52	188.60 (12)
SAR1	512 × 512	7.36	21.72	3.87	480.16 (15)
SAR2	512 × 512	7.38	21.59	3.83	416.97 (13)
SAR3	512 × 512	7.34	21.37	3.38	376.30 (13)
SAR4	512 × 512	7.38	22.21	3.62	446.01 (14)
SAR5	512 × 512	7.31	21.70	3.80	414.39 (13)
SAR6	512 × 512	7.29	21.65	3.37	410.49 (13)
SAR7	512 × 512	7.38	20.76	2.54	319.46 (10)

5. Conclusions

In this paper, we proposed a novel variational model for color image denoising in the presence of mixed multiplicative and Gaussian noise. The proposed formulation combined an infimal-convolution-based data-fidelity term with SVTV and GSR regularization. The data-fidelity term explicitly separated the multiplicative and Gaussian noise components, thereby enabling effective suppression of mixed noise. The two regularization terms served complementary purposes. The SVTV term promoted effective denoising in homogeneous regions and near edges while preserving sharp discontinuities, whereas GSR regularization enhanced reconstruction quality by preserving fine-scale details and textures and alleviating the staircase artifacts caused by SVTV. To solve the resulting nonconvex optimization problem, we employed a PAMA framework to address variable coupling, while convex or nonconvex ADMM schemes were used to efficiently solve the resulting subproblems. This yielded an effective iterative algorithm, and we provided a convergence analysis for the proposed PAMA framework. Numerical experiments demonstrated that the proposed model consistently outperforms existing methods for removing mixed multiplicative and Gaussian noise in color images. Despite its effectiveness, further reduction in computational cost remains an important topic for future research. In particular, the inherently parallel structure of the GSR regularization enables concurrent patch extraction, similarity search, and group-wise sparse coding and SVD. These operations can be independently performed for each group, allowing acceleration on multi-core CPUs and GPUs. In addition, automatic parameter selection schemes, such as spatially adaptive regularization, could be incorporated to further improve reconstruction quality and enhance the preservation of fine details.

Use of AI tools declaration

The author declares he has not used Artificial Intelligence (AI) tools in the creation of this article.

Acknowledgments

This work was supported in part by the National Research Foundation of Korea (RS-2023-00241770) and the Hankuk University of Foreign Studies Research Fund.

Conflict of interest

The author declares no conflict of interest in this paper.

References

1. C. J. Oliver, S. Quegan, *Understanding Synthetic Aperture Radar Images*, Raleigh: SciTech Publishing, 2004.
2. R. F. Wagner, S. W. Smith, J. M. Sandrik, H. Lopez, Statistics of speckle in ultrasound B-scans, *IEEE Trans. Sonics Ultrasonics,* **30** (1983), 156–163. https://doi.org/10.1109/T-SU.1983.31404

3. J. M. Schmitt, S. Xiang, K. M. Yung, Speckle in optical coherence tomography, *J. Biomed. Opt.*, **4** (1999), 95–105. https://doi.org/10.1117/1.429925

4. J. W. Goodman, Some fundamental properties of speckle, *J. Opt. Soc. Amer.*, **66** (1976), 1145–1150. https://doi.org/10.1364/JOSA.66.001145

5. V. S. Frost, J. A. Stiles, K. S. Shanmugan, J. C. Holtzman, A model for radar images and its application to adaptive digital filtering of multiplicative noise, *IEEE Trans. Pattern Anal. Mach. Intell.*, **PAMI-4** (1982), 157–166. https://doi.org/10.1109/TPAMI.1982.4767223

6. K. Krissian, C. F. Westin, R. Kikinis, K. G. Vosburgh, Oriented speckle reducing anisotropic diffusion, *IEEE Trans. Image Process.*, **16** (2007), 1412–1424. https://doi.org/10.1109/TIP.2007.891803

7. S. Parrilli, M. Poderico, C. V. Angelino, L. Verdoliva, A nonlocal SAR image denoising algorithm based on LLMMSE wavelet shrinkage, *IEEE Trans. Geosci. Remote Sens.*, **50** (2012), 606–616. https://doi.org/10.1109/TGRS.2011.2161586

8. G. Aubert, J. F. Aujol, A variational approach to removing multiplicative noise, *SIAM J. Appl. Math.*, **68** (2008), 925–946. https://doi.org/10.1137/060671814

9. J. Shi, S. Osher, A nonlinear inverse scale space method for a convex multiplicative noise model, *SIAM J. Imaging Sci.*, **1** (2008), 294–321. https://doi.org/10.1137/070689954

10. Y. Dong, T. Zeng, A convex variational model for restoring blurred images with multiplicative noise, *SIAM J. Imaging Sci.*, **6** (2013), 1598–1625. https://doi.org/10.1137/120870621

11. L. I. Rudin, S. Osher, E. Fatemi, Nonlinear total variation based noise removal algorithms, *Phys. D: Nonlinear Phenom.*, **60** (1992), 259–268. https://doi.org/10.1016/0167-2789(92)90242-F

12. J. Lu, L. Shen, C. Xu, Y. Xu, Multiplicative noise removal in imaging: An exp-model and its fixed-point proximity algorithm, *Appl. Comput. Harmon. Anal.*, **41** (2016), 518–539. https://doi.org/10.1016/j.acha.2015.10.003

13. W. Wang, M. Yao, M. K. Ng, Color image multiplicative noise and blur removal by saturation-value total variation, *Appl. Math. Model.*, **90** (2021), 240–264. https://doi.org/10.1016/j.apm.2020.08.052

14. M. Jung, Saturation-value based higher-order regularization for color image restoration, *Multidimens. Syst. Signal Process.*, **34** (2023), 365–394. https://doi.org/10.1007/s11045-023-00867-x

15. M. Jung, Group sparse representation and saturation-value total variation based color image denoising under multiplicative noise, *AIMS Math.*, **9** (2024), 6013–6040. https://doi.org/10.3934/math.2024294

16. M. Hintermüller, A. Langer, Subspace correction methods for a class of nonsmooth and nonadditive convex variational problems with mixed L1-L2 data-fidelity in image processing, *SIAM J. Imaging Sci.*, **6** (2013), 2134–2173. https://doi.org/10.1137/120894130

17. A. Langer, Automated parameter selection in the L^1-L^2-TV model for removing Gaussian plus impulse noise, *Inverse Probl.*, **33** (2017), 074002. https://doi.org/10.1088/1361-6420/33/7/074002

18. J. C. De Los Reyes, C. B. Schönlieb, Image denoising: Learning the noise model via nonsmooth PDE-constrained optimization, *Inverse Probl. Imaging*, **7** (2013), 1183–1214. https://doi.org/10.3934/ipi.2013.7.1183

19. A. Jezierska, E. Chouzenoux, J. C. Pesquet, H. Talbot, A convex approach for image restoration with exact Poisson-Gaussian likelihood, *SIAM J. Imaging Sci.*, **62** (2015), 17–30. https://doi.org/10.1137/15M1014395
20. L. Calatroni, C. Chung, J. C. De Los Reyes, C. B. Schönlieb, T. Valkonen, Bilevel approaches for learning of variational imaging models, In: *Variational Methods: In Imaging and Geometric Control*, **18** (2017), 252–290. https://doi.org/10.1515/9783110430394-008
21. L. Calatroni, J. C. De Los Reyes, C. B. Schönlieb, Infimal convolution of data discrepancies for mixed noise removal, *SIAM J. Imaging Sci.*, **10** (2017), 1196–1233. https://doi.org/10.1137/16M1101684
22. L. Calatroni, K. Papafitsoros, Analysis and automatic parameter selection of a variational model for mixed Gaussian and salt-and-pepper noise removal, *Inverse Probl.*, **35** (2019), 114001. https://doi.org/10.1088/1361-6420/ab291a
23. M. Jung, Saturation-value total variation based color image denoising under mixed multiplicative and Gaussian noise, *J. Korean Soc. Ind. Appl. Math.*, **26** (2022), 156–184. https://doi.org/10.12941/jksiam.2022.26.156
24. P. Blomgren, T. F. Chan, Color TV: Total variation methods for restoration of vector-valued images, *IEEE Trans. Image Process.*, **7** (1998), 304–309. https://doi.org/10.1109/83.661180
25. T. Chan, S. Kang, J. Shen, Total variation denoising and enhancement of color images based on the CB and HSV color models, *J. Vis. Commun. Image Represent.*, **12** (2001), 422–435. https://doi.org/10.1006/jvci.2001.0491
26. Z. Jia, M. K. Ng, W. Wang, Color image restoration by saturation-value total variation, *SIAM J. Imaging Sci.*, **12** (2019), 972–1000. https://doi.org/10.1137/18M1230451
27. A. Buades, B. Coll, J. M. Morel, A non-local algorithm for image denoising, In: *2005 IEEE Computer Society Conference on Computer Vision and Pattern Recognition*, San Diego, CA, USA, 2005, 60–65. https://doi.org/10.1109/CVPR.2005.38
28. K. Dabov, A. Foi, V. Katkovnik, K. Egiazarian, Image denoising by sparse 3-d transform-domain collaborative filtering, *IEEE Trans. Image Process.*, **16** (2007), 2080–2095. https://doi.org/10.1109/TIP.2007.901238
29. S. Kindermann, S. Osher, P. W. Jones, Deblurring and denoising of images by nonlocal functionals, *Multiscale Model. Simul.*, **4** (2005), 1091–1115. https://doi.org/10.1137/050622249
30. X. Zhang, M. Burger, X. Bresson, S. Osher, Bregmanized nonlocal regularization for deconvolution and sparse reconstruction, *SIAM J. Imaging Sci.*, **3** (2010), 253–276. https://doi.org/10.1137/090746379
31. M. Jung, X. Bresson, T. F. Chan, L. A. Vese, Nonlocal Mumford-Shah regularizers for color image restoration, *IEEE Trans. Image Process.*, **20** (2011), 1583–1598. https://doi.org/10.1109/TIP.2010.2092433
32. M. Elad, M. Aharon, Image denoising via sparse and redundant representations over learned dictionaries, *IEEE Trans. Image Process.*, **15** (2006), 3736–3745. https://doi.org/10.1109/TIP.2008.2008065
33. J. Mairal, F. Bach, J. Ponce, G. Sapiro, A. Zisserman, Non-local sparse models for image restoration, In: *2009 IEEE International Conference on Computer Vision*, Tokyo, Japan, 2009, 2272–2279. https://doi.org/10.1109/ICCV.2009.5459452

34. W. Dong, L. Zhang, G. Shi, X. Wu, Image deblurring and super-resolution by adaptive sparse domain selection and adaptive regularization, *IEEE Trans. Image Process.*, **20** (2011), 1838–1857. https://doi.org/10.1109/TIP.2011.2108306
35. W. Dong, L. Zhang, G. Shi, X. Li, Nonlocally centralized sparse representation for image restoration, *IEEE Trans. Image Process.*, **22** (2013), 1620–1630. https://doi.org/10.1109/TIP.2012.2235847
36. W. Dong, G. Shi, X. Li, Nonlocal image restoration with bilateral variance estimation: A low-rank approach, *IEEE Trans. Image Process.*, **22** (2013), 700–711. https://doi.org/10.1109/TIP.2012.2221729
37. T. Huang, W. Dong, X. Xie, G. Shi, X. Bai, Mixed noise removal via Laplacian scale mixture modeling and nonlocal low-rank approximation, *IEEE Trans. Image Process.*, **26** (2017), 3171–3186. https://doi.org/10.1109/TIP.2017.2676466
38. X. Liu, J. Lu, L. Shen, C. Xu, Y. Xu, Multiplicative noise removal: Nonlocal low-rank model and its proximal alternating reweighted minimization algorithm, *SIAM J. Imaging Sci.*, **13** (2020), 1595–1629. https://doi.org/10.1137/20M1313167
39. J. Zhang, D. Zhao, W. Gao, Group-based sparse representation for image restoration, *IEEE Trans. Image Process.*, **23** (2014), 3336–3351. https://doi.org/10.1109/TIP.2014.2323127
40. J. Zhang, S. Ma, Y. Zhang, W. Gao, Image deblocking using group-based sparse representation and quantization constraint prior, In: *2015 IEEE International Conference on Image Processing*, Quebec City, Canada, 2015, 306–310. https://doi.org/10.1109/ICIP.2015.7350809
41. W. Shi, C. Chen, F. Jiang, D. Zhao, W. Shen, Group-based sparse representation for low lighting image enhancement, In: *2016 IEEE International Conference on Image Processing*, Phoenix, AZ, USA, 2016, 4082–4086. https://doi.org/10.1109/ICIP.2016.7533127
42. S. Lee, M. Kang, Group sparse representation for restoring blurred images with Cauchy noise, *J. Sci. Comput.*, **83** (2020), 41. https://doi.org/10.1007/s10915-020-01227-8
43. Z. Zha, X. Yuan, B. Wen, J. Zhou, J. Zhang, C. Zhu, A Benchmark for sparse coding: When group sparsity meets rank minimization, *IEEE Trans. Image Process.*, **29** (2020), 5094–5109. https://doi.org/10.1109/TIP.2020.2972109
44. Z. Zha, X. Yuan, B. Wen, J. Zhang, J. Zhou, C. Zhu, Image restoration using joint patch-group based sparse representation, *IEEE Trans. Image Process.*, **29** (2020), 7735–7750. https://doi.org/10.1109/TIP.2020.3005515
45. Z. Zha, X. Yuan, B. Wen, J. Zhou, C. Zhu, Group sparsity residual constraint with non-local priors for image restoration, *IEEE Trans. Image Process.*, **29** (2020), 8960–8975. https://doi.org/10.1109/TIP.2020.3021291
46. Y. Kong, C. Zhou, C. Zhang, L. Sun, C. Zhou, Multi-color channels based group sparse model for image restoration, *Algorithms*, **15** (2022), 176. https://doi.org/10.3390/a15060176
47. Y. Chen, X. Xiao, Y. Zhou, Low-rank quaternion approximation for color image processing, *IEEE Trans. Image Process.*, **29** (2019), 1426–1439. https://doi.org/10.1109/TIP.2019.2941319
48. J. Miao, K. I. Kou, Color image recovery using low-rank quaternion matrix completion algorithm, *IEEE Trans. Image Process.*, **31** (2021), 190–201. https://doi.org/10.1109/TIP.2021.3128321

49. Z. Jia, Q. Jin, M. K. Ng, X. L. Zhao, Non-local robust quaternion matrix completion for large-scale color image and video inpainting, *IEEE Trans. Image Process.*, **31** (2022), 3868–3883. https://doi.org/10.1109/TIP.2022.3176133
50. Y. Yu, Y. Zhang, S. Yuan, Quaternion-based weighted nuclear norm minimization for color image denoising, *Neurocomputing*, **332** (2019), 283–297. https://doi.org/10.1016/j.neucom.2018.12.034
51. C. Huang, Z. Li, Y. Liu, T. Wu, T. Zeng, Quaternion-based weighted nuclear norm minimization for color image restoration, *Pattern Recognit.*, **128** (2022), 108665. https://doi.org/10.1016/j.patcog.2022.108665
52. Q. Zhang, L. He, Y. Wang, L. J. Deng, J. Liu, Quaternion weighted Schatten p-norm minimization for color image restoration with convergence guarantee, *Signal Proc.*, **218** (2024), 109382. https://doi.org/10.1016/j.sigpro.2024.109382
53. I. Csiszár, G. Tusná, Information geometry and alternating minimization procedures, *Stat. Decis.*, **1** (1984), 205–237.
54. H. Attouch, J. Bolte, P. Redont, A. Soubeyran, Proximal alternating minimization and projection methods for nonconvex problems: An approach based on the Kurdyka-Łojasiewicz inequality, *Math. Oper. Res.*, **35** (2010), 438–457. https://doi.org/10.1287/moor.1100.0449
55. J. Bochnak, M. Coste, M. F. Roy, *Real Algebraic Geometry*, Berlin: Springer, 1998. https://doi.org/10.1007/978-3-662-03718-8
56. S. Łojasiewicz, *Introduction to Complex Analytic Geometry*, Basel: Birkhöuser Basel, 1991. https://doi.org/10.1007/978-3-0348-7617-9
57. J. Bolte, A. Daniilidis, A. Lewis, M. Shiota, Clarke subgradients of stratifiable functions, *SIAM J. Optim.*, **18** (2007), 556–572. https://doi.org/10.1137/060670080
58. Y. Wang, W. Yin, J. Zeng, Global convergence of ADMM in nonconvex nonsmooth optimization, *J. Sci. Comput.*, **78** (2019), 1–2. https://doi.org/10.1007/s10915-018-0757-z
59. S. Boyd, N. Parikh, E. Chu, B. Peleato, J. Eckstein, Distributed optimization and statistical learning via the alternating direction method of multipliers, *Found. Trends Mach. Learn.*, **3** (2010), 1–122. https://doi.org/10.1561/2200000016
60. Z. Wang, A. C. Bovik, H. R. Sheikh, E. P. Simoncelli, Image quality assessment: From error visibility to structural similarity, *IEEE Trans. Image Process.*, **13** (2004), 600–612. https://doi.org/10.1109/TIP.2003.819861
61. K. Dabov, A. Foi, V. Katkovnik, K. Egiazarian, Color image denoising via sparse 3d collaborative filtering with grouping constraint in luminance-chrominance space, In: *2007 IEEE International Conference on Image Processing*, San Antonio, TX, USA, 2007, 313–316. https://doi.org/10.1109/ICIP.2007.4378954

AIMS Press